

Belyaeva et al

Cortical actin properties controlled by *Drosophila* Fos

aid macrophage infiltration against surrounding tissue resistance

Short title: Macrophage Cortical Actin counteracts Tissue Resistance

Vera Belyaeva^{§1,2}, Stephanie Wachner^{§1}, Igor Gridchyn^{†1}, Markus Linder^{†3,4}, Shamsi Emtenani¹, Attila Gyoergy¹, Maria Sibilia³, Daria Siekhaus^{1*}

§: These authors contributed equally

†: These authors contributed equally

*- Corresponding author, daria.siekhaus@ist.ac.at

1 – Institute of Science and Technology Austria, Am Campus 1, 3400 Klosterneuburg, Austria

2 – Current address: Molecular Devices, Urstein Süd 17, 5412, Austria

3 – Institute of Cancer Research, Department of Medicine 1, Comprehensive Cancer Center, Medical University of Vienna, Austria

4 – Current address: F. Hoffmann - La Roche Ltd., Grenzacherstrasse 124, 4070 Basel, Switzerland

Belyaeva et al

ABSTRACT

The infiltration of immune cells into tissues underlies the establishment of tissue resident macrophages, and responses to infections and tumors. Yet the mechanisms immune cells utilize to negotiate tissue barriers in living organisms are not well understood, and a role for cortical actin has not been examined. Here we find that the tissue invasion of *Drosophila* macrophages, also known as plasmatocytes or hemocytes, utilizes enhanced cortical F-actin levels stimulated by the *Drosophila* member of the fos proto oncogene transcription factor family (Dfos, Kayak). RNA sequencing analysis and live imaging show that Dfos enhances F-actin levels around the entire macrophage surface by increasing mRNA levels of the membrane spanning molecular scaffold tetraspanin TM4SF, and the actin cross-linking filamin Cheerio which are themselves required for invasion. Cortical F-actin levels are critical as expressing a dominant active form of Diaphanous, a actin polymerizing Formin, can rescue the *Dfos* Dominant Negative macrophage invasion defect. *In vivo* imaging shows that Dfos is required to enhance the efficiency of the initial phases of macrophage tissue entry. Genetic evidence argues that this Dfos-induced program in macrophages counteracts the constraint produced by the tension of surrounding tissues and buffers the mechanical properties of the macrophage nucleus from affecting tissue entry. We thus identify tuning the cortical actin cytoskeleton through Dfos as a key process allowing efficient forward movement of an immune cell into surrounding tissues.

Introduction

The classical model of cell migration on a surface postulated in the 1980's by Abercrombie has been extended (Danuser et al., 2013) by studies showing that migrating cells utilize diverse strategies depending on the architecture and physical properties of their three dimensional (3D) surroundings (Paluch et al., 2016). Much of this work has been

Belyaeva et al

conducted *in vitro*, where variations in the environment can be strictly controlled. However most 3D migration occurs within the body, and much less research has elucidated the mechanisms used to efficiently move in these diverse environments, particularly into and through tissues. Such migration is crucial for the influence of the immune system on health and disease. Vertebrate macrophages migrate into tissues during development where they take up residence, regulating organ formation and homeostasis and organizing tissue repair upon injury (Ginhoux and Guilliams, 2016; Theret et al 2019). A variety of types of immune cells infiltrate into tumors, and can both promote or impede cancer progression (Greten and Grivennikov 2019; Sharma and Allison, 2015). Responses to infection require immune cells to traverse through the vascular wall, into the lymph node, and through tissues (Luster et al., 2005). Yet the mechanisms utilized by immune cells to allow migration into such challenging cellular environments *in vivo* are not well understood.

Migration in 2-D and 3-D environments utilizes actin polymerization to power forward progress. The assembly of actin at the leading edge, when coupled to Integrin adhesion to anchor points in the surrounding ECM, can allow the front of the cell to progress (Mitchison and Cramer, 1996). This anchoring also allows the contraction of cortical actin at the rear plasma membrane to bring the body of the cell forwards. But a role for crosslinked actin at the cell surface in assisting forward progress by helping to counteract the resistance of surrounding tissues and in buffering nuclear properties has not been previously identified.

Our lab utilizes *Drosophila* macrophage migration into the embryonic germband (gb) to investigate mechanisms of immune cell tissue invasion. Macrophages, also called plasmatocytes or hemocytes, are the primary phagocytic cell in *Drosophila* and share striking similarities with vertebrate macrophages (Brückner et al., 2004; Evans & Wood, 2011; Lemaitre & Hoffmann, 2007; Ratheesh et al., 2015; Weavers et al., 2016). They are

Belyaeva et al

specified in the head mesoderm at embryonic stages 4-6 and by stage 10 start spreading along predetermined routes guided by platelet-derived growth factor- and vascular endothelial growth factor-related factors (Pvlf) 2 and 3 (Cho et al., 2002; Brückner et al., 2004; Wood et al., 2006) to populate the whole embryo. One of these paths, the movement into the gb, requires macrophages to invade confined between the ectoderm and mesoderm (Ratheesh et al., 2018; Siekhaus et al., 2010). The level of tension and thus apparent stiffness of the flanking ectoderm is a key parameter defining the efficiency of macrophage passage into and within the gb (Ratheesh et al., 2018). Penetration of macrophages into the gb utilizes Integrin, occurs normally without MMPs (Siekhaus et al., 2010) and is even enhanced by ECM deposition (Valoskova et al., 2019; Sánchez-Sánchez et al., 2017) likely because the basement membrane has not yet formed at this stage (Matsubayashi et al., 2017; Ratheesh et al., 2018). Thus *Drosophila* macrophage gb invasion represents an ideal system to explore the mechanisms by which immune cells and surrounding tissues interact with one another to aid the invasion process.

Here we sought to identify a transcription factor that could control immune cell tissue invasion and elucidate its downstream mechanisms. We identify a role for the *Drosophila* ortholog of the proto-oncogene Fos, in initial entry and migration within the tissue. We find Dfos increases cortical macrophage F-actin levels through the formin Cheerio and the novel target the tetraspanin TM4SF, aiding macrophages to move forward against the resistance of the surrounding tissues while buffering the mechanical properties of the nucleus.

Results

The transcription factor Dfos is required for macrophage germband invasion

To identify regulators of programs for invasion we searched the literature for transcription factors in macrophages prior to or during their invasion of germband tissues (gb) (Fig 1A-B'). Of the 12 such factors (S1 Table, based on Hammonds et al., 2013) we

Belyaeva et al

focused on Dfos, a member of the Fos proto-oncogene family, assigned by the Roundup algorithm as being closest to vertebrate c-fos (Deluca et al., 2012; Thurmond et al., 2019) (Fig 1C). Dfos contains the basic leucine zipper domain (bZIP) shown to mediate DNA binding and hetero and homo dimerization (Glover and Harrison, 1995; Szalóki et al., 2015) with the third leucine replaced by a methionine, a position also altered in the *C. elegans* ortholog FOS-1A (Sherwood et al., 2005). Embryo *in situ* hybridizations reveal enriched expression of the gene in macrophages at early stage 11 (Fig 1D, arrow) which is attenuated by stage 13. Dfos protein appears in the nucleus in a subset of the macrophages that are migrating towards the gb at stage 10-11 and in all macrophages by early stage 12 (Fig 1E-F' yellow arrowheads, G-G''' white arrows) persisting through stage 13 (S1A Fig). The *Dfos*¹ null mutant eliminates the macrophage signal, indicating antibody specificity (Fig 1H). To determine if Dfos affects invasion, we examined the 70% of embryos from *Dfos*¹ and the hypomorph *Dfos*² that did not display developmental defects at these early stages; we quantified macrophage numbers in the gb during a defined development period in early stage 12 (Fig 1M). Both Dfos mutants displayed significantly reduced numbers of macrophages in the gb compared to the control (Fig 1I-K, N) with normal numbers in the pre-gb zone for *Dfos*² (S1B Fig) (S1 Data). Macrophage-specific expression of *Dfos* rescues the *Dfos*² mutant (Fig 1L,N). Blocking Dfos function in macrophages with a dominant negative (DN) Dfos (Fig 1O-Q) that lacks the activation domain but retains the capacity to dimerize and bind DNA (Eresh et al., 1997) or two different RNAis against *Dfos* (Fig 1R) recapitulates the decrease in gb macrophages seen in the null while not affecting macrophage numbers in the whole embryo (S1C Fig), neighboring the germband (S1D Fig) and along the ventral nerve cord (vnc); (S1E-F Fig). These results argue that Dfos is required in macrophages for their migration into the gb. Since overexpressing DfosDN in the midgut does not inhibit a bZIP protein that acts there (Eresh et al., 1997) and

Belyaeva et al

overexpressing Dfos in macrophages does not change gb numbers (S1G Fig), Dfos and DfosDN do not appear to inhibit other bZIP proteins at higher levels of expression. As DfosDN should exert a quicker effect than RNAis, further experiments examining Dfos' role in enhancing germband invasion utilized mostly the DN form.

Fig 1. The bZIP transcription factor Dfos acts in macrophages to facilitate their migration into the germband

Schematics of lateral (A) stage (St) 11 and (A') early St 12 embryos. The boxed region magnified below indicates where macrophages (green) invade the germband (gb) after moving there from the head (B-B'). Macrophages sit on the yolk sac (yellow) next to the amnioserosa (black line) and then invade between the ectoderm (blue) and mesoderm (purple).

(C) Dfos protein aligned with its human orthologs c-Fos and FosB; orange outlines the bZIP region that has 48% identity to both proteins; identical amino acids shown in orange, conserved ones in green. Stars indicate Leucines in the zipper; ^ the third leucine which in Dfos is a methionine, a tolerated substitution (Garcia-Echeverria, 1997). The lower solid line indicates the basic domain and the dotted line the leucine zipper (ZIP).

(D) *In situ* hybridization of St 11 and 13 embryos with a riboprobe for Dfos-RB (Fbcl0282531) which also detects all Dfos isoforms. *Dfos* RNA expression is enriched in macrophages (arrow) and the amnioserosa (arrowhead) before gb invasion, but is gone thereafter.

(E-H') Confocal images of the boxed region in A from fixed embryos expressing *GFP* in macrophages (green) stained with a Dfos Ab (red). (E-F', H-H') A white dashed line indicates the gb edge. (E-F) The Dfos Ab (yellow arrowheads) stains (E) a subset of the macrophages moving towards the gb at St 11, and (F) all macrophages by early St 12, as well as the amnioserosa (white arrowheads). (G) Higher magnification shows Dfos colocalizing with the nuclear marker DAPI (white). (H) No staining is detected in macrophages or the amnioserosa in the null *Dfos*¹ mutant.

(I-L) Lateral views of mid St 12 embryos from (I) the control, (J) the null allele *Dfos*¹, (K) the hypomorphic allele *Dfos*², and (L) *Dfos*² with *Dfos* re-expressed in macrophages.

Belyaeva et al

(M) Schematic of St 12 embryo, gb region indicated by a black oval outline. (N) Quantitation reveals that both *Dfos* alleles display fewer macrophages in the gb. Re-expression of *Dfos* in macrophages in the *Dfos*² hypomorph significantly rescues the defect. Control vs. *Dfos*¹ p=0.02 (30% reduction), Control vs. *Dfos*² p=0.017 (25% reduction), Control vs. *Dfos*²; *mac>Dfos* p=0.334.

(O-P) Lateral views of mid St 12 embryos from (O) the control, or (P) a line expressing a dominant negative (DN) form of *Dfos* in macrophages. (Q) Quantification of macrophage numbers in the gb (see schematic) in the two genotypes visualized in O, P. p<0.0001(****) (41% reduction).

(R) Quantification of macrophage numbers in the gb of the control and two different lines expressing RNAi constructs against *Dfos* in macrophages. Control vs. *Dfos* RNAi¹ (TRiP HMS00254) p=0.001 (32% reduction), Control vs. *Dfos* RNAi² (TRiP JF02804) p=0.02 (21% reduction). The data in Q and R argue that *Dfos* is required within macrophages to promote gb tissue invasion.

Embryos are positioned with anterior to left and dorsal up in all images and histograms show mean + standard error of the mean (SEM) throughout. Macrophages are labeled using *srp-Gal4* (“mac>”) driving *UAS-GFP* in E-H, *UAS-GFP::nls* in I-L and *srpHemo-H2A::3xmCherry* in O-P. ***p<0.005, **p<0.01, *p<0.05. One-way ANOVA with Tukey post hoc was used for N and R, and unpaired t-test for Q. The embryo number analysed is indicated within the relevant column in the graphs. Scale bar: 50 μm in D, 5 μm in E-H and 10 μm in I-L, O-P.

Dfos promotes macrophage motility and persistence during tissue entry

To examine the dynamic effects of *Dfos* on tissue invasion, we performed live imaging and tracking of macrophages. We visualized macrophages with *srpHemo-H2A::3xmCherry* (Gyoergy et al., 2018) in either a wild type or *mac>DfosDN* background, capturing the initial stage of invasion (S1 Movie). The speed of macrophages moving in the area neighboring the germband prior to invasion was not significantly changed (pre-gb, Fig 2B,C). However, the first *mac>DfosDN* macrophage to enter is delayed by 20 min in crossing into the gb (Fig 2D). *mac>DfosDN* macrophages also displayed reduced speed and directional persistence during entering as well as while moving along the first 20μm of the

Belyaeva et al

ectoderm-mesoderm interface (gb entry, Fig 2E, S2A Fig). Macrophages in the *Dfos*² mutant largely mirrored this phenotype, but displayed slower movement in the pre-gb zone neighboring the amnioserosa in which *Dfos* is also expressed (Fig 1D-F), likely causing a non-autonomous effect (S2B-C Fig, S2 Movie) (Fig 1D, black arrowhead, E-F, white arrowheads). Macrophages expressing *Dfos*DN moved with unaltered average speed as they spread out along the non-invasive route of the vnc (Fig 2F, Fig 2G, S3 Movie), albeit with reduced directional persistence (S2A Fig). We thus conclude from live imaging that *Dfos* in macrophages aids their initial invasive migration into the gb, increases their speed within the gb and does not underlie their progress along the vnc.

Fig 2. *Dfos* facilitates the initial invasion of macrophages into the gb tissue

(A) Movie stills of control embryos and those expressing *Dfos*DN in macrophages (green, labelled using *sprHemo-H2A::3xmCherry*). Area imaged corresponds to the black dashed square in the schematic above. The germband (gb) border is outlined with a white dashed line. The first entering macrophage is indicated with a white arrowhead, and time in minutes in the upper right corner.

(B) Detailed schematic showing the different zones for which the parameters of macrophage gb invasion were quantified. The pre-gb area is shown in yellow, the gb entry zone is outlined in a solid line.

(C) Macrophage speed in the pre-gb area was not significantly changed in macrophages expressing *Dfos*DN ($3.00 \mu\text{m}/\text{min}$) compared to the control ($3.61 \mu\text{m}/\text{min}$), $p = 0.58$.

(D) Quantification shows a 68% increase in the total gb crossing time of *Dfos*DN expressing macrophages compared to the control. Total gb crossing time runs from when macrophages have migrated onto the outer edge of the gb ectoderm, aligning in a half arch, until the first macrophage has translocated its nucleus into the gb ecto-meso interface. $p = 0.008$.

(E) *Dfos*DN expressing macrophages displayed a significantly reduced speed ($1.53 \mu\text{m}/\text{min}$) at the gb entry zone compared to the control ($1.98 \mu\text{m}/\text{min}$), $p = 1.11 \times 10^{-6}$.

(F) Macrophages expressing *Dfos*DN in a Stage 13 embryo move with unaltered speed along the vnc in the region outlined by the dashed black box in the schematic above (4.93

Belyaeva et al

$\mu\text{m}/\text{min}$), compared to the control ($4.55 \mu\text{m}/\text{min}$), $p = 0.64$. Corresponding stills shown in (G) Macrophages are labeled by *srpHemo-Gal4* driving *UAS-GFP::nls*. *** $p < 0.005$, ** $p < 0.01$, * $p < 0.05$. Unpaired t-test used for C-F, a Kolmogorov-Smirnov test for D. For each genotype, the number of tracks analysed in C and F, and the number of macrophages in D-E are indicated within the graph columns. Tracks were obtained from movies of 7 control and 7 *mac>DfosDN* expressing embryos in panel D, 3 each in C, F, and 4 each in E. Scale bar: $10 \mu\text{m}$.

Dfos modulates Filamin and Tetraspanin to aid gb tissue invasion

To identify Dfos targets that promote macrophage invasion, we FACS isolated macrophages from wild type and *mac>DfosDN* embryos during the time when invasion has just begun, and conducted RNA-sequencing of the corresponding transcriptomes (Fig 3A, S1 Data). We first assessed reads that map to Dfos, which can correspond to both endogenous and DfosDN mRNA; we found a 1.6 fold increase in the presence of the one copy of DfosDN in this line, arguing that this transgene is expressed at levels similar to each endogenous copy of Dfos and is unlikely to produce extraneous effects (S2 Data). We then examined genes that in the presence of DfosDN displayed a log2 fold change of at least 1.5 with an adjusted P value less than 0.05. 10 genes were down-regulated (Fig 3B, S3A-B Fig) and 9 up-regulated by DfosDN (S2 Table). Upregulated genes in DfosDN encoded mostly stress response proteins, so we concentrated on the downregulated class. Of these, we focused on the actin crosslinking filamin Cherio (Cher) and the tetraspanin TM4SF from a group that can form membrane microdomains that affect signalling and migration (Razinia et al., 2012; Yeung et al., 2018). No known role for TM4SF had been previously identified in *Drosophila*. To determine if these Dfos targets were themselves required for invasion, we RNAi knocked down Cher and TM4SF through RNAi individually or simultaneously and observed significantly reduced macrophage numbers in the gb, particularly upon the knockdown of both targets simultaneously (Fig 3C-G) while not affecting macrophage numbers in the pre-gb zone (S3D Fig) or on the vnc (S3E Fig). Over-expression of Cher or TM4SF along with

Belyaeva et al

DfosDN in macrophages increased the mean macrophage numbers in the gb, and over-expression of TM4SF rescued the *DfosDN* macrophage invasion defect (Fig 3H-L). Expression of a GFP control did not restore macrophage invasion indicating that the rescue we observed through Cher or TM4SF expression was not due to promoter competition leading to reductions in *DfosDN* expression. We conclude that *Dfos* aids macrophage gb invasion by increasing the mRNA levels of the filamin actin crosslinker Cher and the tetraspanin TM4SF.

Fig 3. *Dfos* regulates macrophage germband invasion through cytoskeletal regulators the Filamin Cheerio and the tetraspanin TM4SF

(A) Schematic representing the pipeline for analyzing mRNA levels in FACS sorted macrophages.

(B) Table of genes down-regulated in macrophages expressing *DfosDN*. Genes are ordered according to the normalized p-value from the RNA-Sequencing. The closest mouse protein orthologs were found using UniProt BLAST; the hit with the top score is shown in the table.

(C-F) Lateral views of representative St 12 embryos in which the two targets with links to actin organization, **(D)** the Tetraspanin TM4SF and **(E)** the Filamin Cheerio, have been knocked down individually or **(F)** together, along with the control **(C)**. Scale bar: 50 μ m.

(G) Quantification shows that the number of macrophages in the germband is reduced in embryos expressing RNAi against either *cher* (*KK 107451*) or *TM4SF* (*KK 102206*) in macrophages, and even more strongly affected in the double RNAi of both. Control vs. *cher* RNAi p=0.0005 (46% reduction). Control vs. *TM4SF* RNAi p=0.009 (37% reduction), Control vs. *cher/TM4SF* RNAi p>0.0001 (61% reduction). *cher* RNAi vs. *TM4SF* RNAi p=0.15.

(H-K) Lateral views of a representative St 12 embryo from **(H)** the control, as well as embryos expressing *DfosDN* in macrophages along with either **(I)** GFP, **(J)** Cher, or **(K)** TM4SF.

(L) Quantification shows that over-expression of TM4SF in *DfosDN* expressing macrophages restores their normal numbers in the gb. Over-expression of Cher in this background shows a strong trend towards rescue, but did not reach statistical significance. Control vs. *DfosDN* p=0.015 (28% reduction); Control vs. *cher* p=0.74; Control vs. *TM4SF*

Belyaeva et al

p>0.99; *DfosDN* vs. *DfosDN cher* p=0.14; *DfosDN* vs. *DfosDN, TM4SF* p<0.0001; Control vs. *cher* p=0.97; Control vs. *TM4SF* p=0.35.

(M-O) q-PCR analysis of mRNA extracted from the bones of mice that are wild type, transgenic (tg) for *Fos* controlled by a Major Histocompatibility promoter and viral 3'UTR elements, and those in which such c-Fos transgenesis has led to an osteosarcoma (OS). Analysis of mRNA expression shows that higher levels of **(M)** *Fos* correlate with higher levels of **(N-N')** *Flna-C*, and **(O)** *Tspan6* in osteosarcomas. p values = 0.86, 0.001, 0.003 in **M**, 0.98, 0.009, 0.007 in **N**, 0.39, < 0.0001, <0.0001 in **N'**, 0.76, 0.005, 0.002 in **N''**, 0.99, 0.004, 0.003 in **O**. Scale bar: 50 μ m.

Macrophages are labeled using either **(C-F)** *srp::H2A::3xmCherry* or **(H-K)** *srpHemo-Gal4* ("mac>") driving *UAS-mCherry::nls*. ***p<0.005, **p<0.01, *p<0.05. Unpaired t-test or one-way ANOVA with Tukey post hoc were used for statistics. Each column contains the number of analyzed embryos.

In murine osteosarcoma c-fos mRNA level increases correlate with those of Filamins and Tetraspanin-6

To determine if these *Dfos* targets in *Drosophila* could also be *Fos* targets in vertebrate cells, we utilized a well-established murine transgenic model that over expresses c-fos. In these mice transgenic c-fos expression from viral 3' UTR elements in osteoblasts (the bone forming cells) leads to osteosarcoma development accompanied by a 5 fold increase in c-fos mRNA expression (Fig 3M) (Linder et al., 2018). We examined by qPCR the mRNA levels of our identified *Dfos* targets' orthologs, comparing their levels in osteosarcomas (*Fos* tg OS) to neighboring, osteoblast-containing healthy bones from *Fos* tg mice (*Fos* tg bone) and control bones from wild-type mice (wt bone). We saw 2.5 to 8 fold higher mRNA levels of the three murine Filamin orthologs (Fig 3N-N') and a 15 fold increase in Tetraspanin-6 (Fig 3O) in osteosarcoma cells. mRNA levels of several of the orthologs of other *Dfos* targets we had identified showed less strong inductions or even decreases; the Glutathione S transferase *Gstt3* and the Slit receptor *Evalc* increased 4 and 2.8 fold respectively, while the mitochondrial translocator *Tspo* was 25% lower (S3F-I Fig). These results suggest that

Belyaeva et al

Dfos's ability to increase mRNA levels of two key functional targets for migration, a Filamin and a Tetraspanin, is maintained by at least one vertebrate fos family member.

Dfos increases cortical actin polymerization through Cheerio and TM4SF to aid macrophage invasion

We wished to determine what cellular properties Dfos could affect through such targets to facilitate *Drosophila* macrophage invasion. Given Cheerio's known role as an actin crosslinker, we examined actin in invading *mac>DfosDN* macrophages within live embryos. To visualize actin in macrophages, we utilized a *srpHemo-moe::3xmCherry* reporter which marks cortical F-actin (Edwards et al., 1997; Franck et al., 1993) and observed a reduction of 53% (Fig 4A-D) in invading *mac>DfosDN* macrophages. We hypothesized that these changes in actin all around the cell edge could be due to the lower levels of Cheerio and/or TM4SF mRNA in the *mac>DfosDN* macrophages. Indeed, we observed reductions in *moe::3xmCherry* all around the edge of invading macrophages in live embryos expressing RNAi against Cher or TM4SF in macrophages, (Fig 4E-H). To test if a decrease in actin assembly could underlie the reduced tissue invasion of *mac>DfosDN* macrophages, we forced cortical actin polymerization by expressing a constitutively active version of the formin Diaphanous (Dia-CA) which localizes to the cortex (Gonzalez-Gaitan and Peifer, 2009). Indeed, Dia-CA completely rescued the *DfosDN* invasion defect (Fig 4I-J). Given that Dia, like Dfos, does not affect general macrophage migratory capacities along the ventral nerve cord (Davis et al., 2015), we examined if Dia might normally play a role in invasion. We utilized two RNAis against Dia and observed decreased macrophage numbers in the gb in each (Fig 4K-L) with no effect on numbers in the pre-gb (S4A Fig) or on the vnc (S4B Fig). These results argue that Dfos aids invasion by increasing levels of TM4SF and Cheerio to

Belyaeva et al

enhance actin polymerization around the surface of the macrophage, potentially by increasing the activity of Dia.

Fig 4. Dfos regulates the actin cytoskeleton through Cher, TM4SF, and the formin Diaphanous

(A) Quantification of phalloidin intensity to detect F actin at the macrophage-macrophage contacts in Stage 11/12 *Dfos*^l embryos. F-actin is strongly reduced at these homotypic contacts.

(B-C, F-H) Representative confocal images of live embryos expressing in invading macrophages the F-actin binding and homodimerizing portion of Moesin (*srpHemo-moe::3xmCherry*) to label F-actin. Relative Moe-3xmCherry intensity is indicated with a pseudo-color heat map as indicated on the left, with yellow as the highest levels and dark blue as the lowest.

(D-E) Quantification of the macrophage Moe:3xmCherry intensity as a measure of cortical F-actin, normalized to the average fluorescence intensity of the control per batch.

(D) Quantification shows that macrophages expressing DfosDN display a 53% reduction in Moe::3xmCherry intensity compared to the control when the two outliers shown as single dots are excluded, 37% if they are included. Outliers identified by 10% ROUT. n of ROIs analysed = 650 for control, 687 for *DfosDN*. p=0.0007 for analysis including outliers (Kolmogorov-Smirnov) and p<0.0001 for analysis excluding outliers (Welch's t-test).

(E) Quantification reveals that macrophage expression of an RNAi against either *cher* or *TM4SF*, the two genes whose expression is reduced in *DfosDN*, also results in a decrease of Moe::3xmCherry intensity (by 40% each). n of ROIs analysed = 549 for control, 423 for *cher RNAi*, 306 for *TM4SF RNAi*. Control vs. *cher RNAi* p=0.006. Control vs. *TM4SF* p=0.003.

(I,I') Representative confocal images of St 12 embryos from the control and a line in which macrophages express DfosDN and a constitutively active (CA) form of the formin Dia to restore cortical actin polymerization.

(J) Quantification shows that while macrophage expression of DiaCA does not significantly affect the number of macrophages in the gb, expressing it in a DfosDN background rescues that lines' macrophages gb invasion. Control vs. *DfosDN* p=0.017 (28% reduction), Control vs. *diaCA* p=0.18, Control vs. *DfosDN, diaCA* p=0.010, *DfosDN* vs. *DfosDN, diaCA* p<0.0001

(K,K') Representative confocal images of St 12 embryos from the control and from a line expressing an RNAi against *dia* in macrophages.

(L) Quantification of two RNAi lines against *dia* expressed in macrophages shows a 37% and 21% reduction in macrophage numbers in the gb compared to control. Control vs. *dia RNAi*¹ (TRiP HMS05027) p<0.0001; control vs. *dia RNAi*² (TRiP HMS00308) p=0.0008.

Belyaeva et al

Macrophages are labeled using either *srpHemo-Gal4* driving *UAS-mCherry::nls* (**I-I'**), or *srpHemo-H2A::3xmCherry* (**K-K'**). *srpHemo-moe::3xmCherry*, *srpHemo-Gal4* crossed to (**B**) *UAS-GFP* as a Control, (**C**) *UAS-DfosDN*, (**F**) w⁻ Control, (**G**) *UAS-cher RNAi* (KK 107451), or (**H**) *UAS-TM4SF RNAi* (KK 102206). ***p<0.005, **p<0.01, *p<0.05. Unpaired t-test used for **A**, one way ANOVA with Tukey post hoc for **E, J, L** and Welch's t test of normalized average mean intensity per embryo for **D** with the two indicated outliers excluded, for statistical assessment. The number of analyzed (**A**) macrophage-macrophage junctions, or (**D-E, J, L**) embryos is shown in each column. Scale bar 10 μ m in (**B-C, F-H**), 50 μ m in (**I, K**).

We examined what consequence these lower cortical F-actin levels had on the cellular behavior of macrophages during entry. Quantitation showed that the actin protrusion that macrophages initially insert between the ectoderm and mesoderm during invasion was actually longer in the *mac>DfosDN>LifeAct::GFP* macrophages than in the control (Fig 5A, S5A Fig, S4 Movie). We then performed live imaging of macrophages labeled with CLIP::GFP to visualize microtubules and thus cell outlines in both genotypes; we determined the aspect ratio (maximal length over width) that the first entering cell displays as it enters into the gb. The first *DfosDN*-expressing macrophage was extended even before it had fully moved its rear into the gb (S5B Fig). We carried out measurements, taking only cells that had entered the gb to be able to clearly distinguish the rear of the macrophage from following cells (Fig 5B). We also avoided including in this measurement the forward protrusion and determined that the first macrophage inside the gb displays an average increase of 23% in the maximal length (L) of the cell body and a 12% reduction in the maximal width (W) (S5 Fig). Interestingly, in the pre-gb zone the aspect ratio (max L/W) of *mac>DfosDN* macrophages was not different from control macrophages (Fig 5C-D) although the *mac>DfosDN* cells were 9% smaller in both their length and width (S5D Fig). This suggested that the gb could impose resistance on the entering macrophage, an effect which *mac>DfosDN* macrophages have trouble overcoming due to their compromised actin cytoskeleton at the cortex.

Belyaeva et al

Fig 5. Dfos aids macrophage gb invasion against the resistance of surrounding tissues and buffers the nucleus

(A) Quantification from live embryos shows that the length of the F-actin protrusion of the first entering macrophage is longer in macrophages expressing DfosDN. $p=0.011$. The F-actin protrusion labelled with *srpHemo-Gal4* driving *UAS-LifeAct::GFP* was measured in the direction of forward migration (see schematic).

(B-C) Stills from 2-photon movies of St 11 embryos showing (B) the first macrophages entering the gb and (C) macrophages in the pre-gb zone in the control and in a line expressing DfosDN in macrophages. Microtubules are labelled with *srpHemo-Gal4* driving *UAS-CLIP::GFP*. A blue arrow indicates the front and a yellow arrow indicates the rear of the macrophage. Schematics above indicate where images were acquired

(D) Schematic at left shows macrophage measurements: vertical line for the maximum length and horizontal line for the maximum width. Histograms show the probability density distributions of the aspect ratios (maximum length over maximum width) of the first macrophage entering the gb (left) and macrophages in the pre-gb (right). Macrophages expressing *DfosDN* are more elongated the *mac>DfosDN* line. Control vs. *DfosDN* aspect ratios at gb entry $p=0.0004$, in pre-gb $p=0.39$.

Confocal images of St 12 embryos expressing RNAi against Lamin or LaminC in macrophages in (E-E''') the control, or (F-F''') in embryos also expressing DfosDN in macrophages. *srpHemo-GAL4* used as drover. *Lam RNAi¹*: GD45636; *RNAi²*KK107419. *Lam C RNAi*: TRiP JF01406

(G) Macrophage RNAi knockdown of Lamins which can increase nuclear deformability did not affect macrophages numbers in the gb in the control. In embryos in which macrophages expressed DfosDN, Lamin knockdown rescues their reduced numbers in the gb. Control vs. *DfosDN* $p<0.0001$. Control vs. *Lam RNAi¹* $p>0.99$, vs. *Lam RNAi²* $p=0.83$, vs. *LamC RNAi* $p>0.99$. Control vs. *DfosDN*, *Lam RNAi¹* $p=0.024$, vs. *DfosDN*, *Lam RNAi²* $p>0.99$, vs. *DfosDN*, *LamC RNAi* $p>0.99$. *DfosDN* vs. *DfosDN*, *Lam RNAi¹* $p<0.0001$, vs. *DfosDN*, *Lam RNAi²* $p=0.0049$, vs. *DfosDN*, *LamC RNAi* $p<0.0001$.

(H) Expressing *DfosDN* in macrophages reduces their number in the gb. Concomitantly reducing tissue tension in the ectoderm (light blue in schematic) through Rho1DN substantially rescues invasion. *srpHemo-QF QUAS* control (*mac<>*) governed macrophage expression and *e22C-GAL4* ectodermal (*ecto>*). Control vs. *mac<>DfosDN* $p<0.0001$ (56% reduction), vs. *mac<>DfosDN*; *ecto>Rho1DN* $p>0.99$, vs. *ecto>Rho1DN* $p=0.11$. *mac<>DfosDN* vs. *mac<>DfosDN*; *ecto>Rho1DN* $p<0.0001$, vs. *ecto>Rho1DN* $p=0.0044$. *mac<>DfosDN*; *ecto>Rho1DN* vs. *ecto>Rho1DN* $p>0.99$.

Belyaeva et al

Macrophages are labeled in **B-C** by *srp-Gal4* driving *UAS-CLIP::GFP*, and in **E-F** by *srpHemo-Gal4 UAS-mCherry-nls*. *** $p < 0.005$, ** $p < 0.01$, * $p < 0.05$. Unpaired t-test was used for **A**, one way ANOVA with Tukey post hoc for **G, H**. The number shown within the column corresponds to measurements in **A**, and analysed embryos in **G, H**. Scale bar 5 μ m in **B-C**, and 50 μ m in **E-F**.

Dfos promotes advancement of macrophages against the resistance of the surrounding tissues and buffers the nucleus

We therefore examined how the properties of the gb tissues and macrophages interact during invasion. We first investigated if the macrophage nucleus impedes normal invasion by varying levels of the two *Drosophila* Lamin genes, Lam and LamC, both equally related to the vertebrate lamins A and B1 (Muñoz-Alarcón et al., 2007) and both shown to affect nuclear stiffness and deformability (Wintner et al., 2020; Zwerger et al., 2013). Over-expressing Lam (S5E Fig) or knocking down either of these Lamins in macrophages through RNAi (Perkins et al., 2015) did not change macrophage numbers in the gb of wild type embryos (Fig 5E-E'', G), suggesting that the stiffness of the macrophage nucleus is not a rate limiting parameter during normal tissue invasion into the narrow path between the ectoderm and mesoderm. This result also argues that Lamins' capacity to alter gene expression is not normally important for invasion (Andrés & González, 2009). However in *mac>DfosDN* macrophages, knockdown of these Lamins was able to rescue the gb invasion defect (Fig 5E-G), supporting the conclusion that the properties of the nucleus affect invasion in the absence of the higher levels of cortical actin Dfos normally induces. To directly test if reducing the tension of surrounding tissues can counteract the absence of Dfos, we expressed Rho1DN in the ectoderm with the *e22C-GAL4* driver while expressing *QUAS-DfosDN* in macrophages with the GAL4-independent Q-system driver we had constructed, *srpHemo-QF2* (Gyoergy et al., 2018). Rho1 through ROCK is a key regulator of Myosin activity, epithelial tension and tissue stiffness (Warner & Longmore, 2009; Zhou et al., 2009); Myosin II is essential for actin contractility (Heer & Martin, 2017) and tension

Belyaeva et al

in the *Drosophila* gb ectoderm (Ratheesh et al., 2018). Indeed, we found that this reduction of ectodermal tension substantially rescued *DfosDN* expressing macrophage numbers in the gb (Fig 5H). Taken together our results argue that *Dfos* aids *Drosophila* macrophages in withstanding the resisting force of surrounding cells against the nucleus during invasion into tissues.

Discussion:

We identify the ability to tune the state of the cortical actin cytoskeleton as a key capacity for immune cells migrating into and within tissue barriers *in vivo*. We find that macrophages upregulate a program governed by the transcription factor *Dfos* to enable this. *Dfos* in *Drosophila* is known to regulate the movement during dorsal or wound closure of epithelial sheets (Brock et al., 2012; Lesch et al., 2010; Riesgo-Escovar & Hafen, 1997; Zeitlinger et al., 1997) as well as the development of epithelial tumors and their dissemination (Külshammer et al., 2015; Uhlirova & Bohmann, 2006; Külshammer & Uhlirova, 2013; Benhra et al., 2018). Here we define a different role, namely that *Dfos* enables a stream of individual immune cells to efficiently push their way into tissues, a process which is aided rather than hampered by the presence of the ECM (Sánchez-Sánchez et al., 2017; Valoskova et al., 2019). This function appears specifically required for invasion as we observe no defects in *DfosDN* macrophages' migratory speed in open environments. *DfosDN* macrophages display decreased actin at the cell edge and an elongated shape within the germband, suggesting a defect in the stiffness of the cortex. Indeed, only in the presence of *DfosDN* does the state of the nucleus become relevant, with reductions in Lamins shown to underlie nuclear stiffness (Wintner et al., 2020) enhancing the ability of macrophages to invade. These findings along with the ability of a softened ectoderm to substantially rescue the *DfosDN* macrophages' germband invasion defect lead us to propose the model (Fig 6)

Belyaeva et al

that Dfos permits efficient initial translocation of the macrophage body under ectodermal reactive load by forming a stiff cortical actin shell that counteracts surrounding tissue resistance and protects the nucleus from undergoing high levels of mechanical stress during its deformation.

Fig. 6. Model: Dfos increases actin assembly and crosslinking through the tetraspanin TM4SF and the Filamin Cheerio to counter surrounding tissue resistance

We propose a model for how Dfos tunes the cortical actin properties of *Drosophila* embryonic macrophages to aid their infiltration against the resistance of the surrounding germband tissue. Dfos leads to an increase of the tetraspanin TM4SF and the Filamin Cheerio (Cher). The binding of TM4SF and Filamin to different partners (see Figure S6) forms a network at the cell surface of Integrin, actin and upstream signaling molecules; this results in the recruitment of Rho GEFs and activation of Rho GTPases and the formin Diaphanous, which can stimulate further actin polymerization. Thereby, F-actin is assembled into a more crosslinked and dense network aiding the macrophage in moving its cell body into the ecto-meso interface. The presence of Lamin around the nuclear membrane does not affect this process in the wildtype. However, in the DfosDN-expressing macrophages, the loss of Cher and TM4SF lead to reduced cross-linked actin levels at the cell cortex making the stiffness of the nucleus the rate limiting step for macrophage infiltration of the gb tissue.

A molecular program for tissue invasion that strengthens cortical actin

Crucial mediators of this process are two actin regulators, the filamin Cher, known to be a Dfos target in epithelia, and the previously uncharacterized membrane scaffold tetraspanin TM4SF. We show that both require Dfos for higher mRNA levels in macrophages and present correlative evidence that these classes of genes are also upregulated by vertebrate c-fos. Each of these Dfos targets is required for macrophage invasion; over-expression of TM4SF in macrophages can rescue the *DfosDN* tissue invasion phenotype. We propose that these targets act together to tune the actin cytoskeleton for tissue invasion. Higher Filamin levels cross-link actin filaments into resilient and stiffer networks maintaining cell integrity during mechanical stress (Goldmann et al., 1997; Tseng et al., 2004; Fujita et al., 2012). This aids the distribution of forces from focal adhesions

Belyaeva et al

across the entire migrating cell body, since Filamins can bind directly to Integrin, and even more strongly under strain (Ehrlicher et al., 2011; Glogauer et al., 1998; Kumar et al., 2019; Razinia et al., 2012). Tetraspanins, self-associating multipass transmembrane proteins, also can bind Integrin, forming microdomains of adhesion molecules, receptors and their intracellular signaling complexes, including Rho GTPases (Zimmerman, et al., 2016; Termini & Gillette, 2017; Yáñez-Mó et al., 2009; Berditchevski & Odintsova, 1999). Filamins similarly bind receptors, regulators of actin assembly, Rho GTPases and the Rho GEF Trio (Popowicz et al., 2006; Stossel et al., 2001; Vadlamudi et al., 2002; Ohta et al., 1999; Bellanger et al., 2000). Given that we observe reduced macrophage cortical F-actin in the absence of either the Filamin Cheerio or the Tetraspanin TM4SF we propose that these targets enhance the recruitment and activation of Rho GTPases and the formin Dia to stimulate actin polymerization (Fig 6, S6 Fig) (Rousso et al., 2013; Seth et al., 2006; Großhans et al., 2005; Williams et al., 2007; Delaguillaumie et al., 2002). *Dfos*' upregulation of both targets could thus lead to a supra-network in which ECM-anchored FAs connect to a strong cross-linked cortical actin lattice, allowing Myosin contraction to be converted into cellular advancement despite resistance from the flanking ectoderm.

We demonstrate that the actin nucleating formin Dia is important for *Drosophila* macrophage invasion and capable of rescuing the defects in the *DfosDN* mutant. Unlike the formin Ena which mediates chemotaxis (Davidson et al., 2019), Dia is not required for general *Drosophila* macrophage migration, and instead allows macrophages to recoil away from one another (Davis et al., 2015). Dia could be required for macrophages specifically when they face resistance from their surroundings. Modeling indicates that Dial's regulation of cortical tension requires an optimal combination of actin cross linking and intermediate actin filament length (Chugh et al., 2017). *Drosophila* Dia is a more processive nucleator than Ena (Bilancia et al., 2014) and thus could create the intermediate length actin filaments

Belyaeva et al

that enable higher levels of macrophage cortical tension and strain stiffening (Kasza et al., 2010) on all sides of the cell during their invasion.

Our findings thus demonstrate that there are commonalities in the molecular mechanisms by which *Drosophila* cells invade into either confluent tissues or the ECM. Dfos's upregulation of the Filamin Cheerio is also required in tumor cells and aneuploid epithelial cells to enhance ECM breaching (Külshammer & Uhlirova, 2013; Benhra et al., 2018). Both cell types displayed enhanced levels of cortical filamentous actin, which in the tumors is concomitant with Dia upregulation (Külshammer & Uhlirova, 2013). In the oocyte, Filamin is required for follicle cell intercalation and border cells display higher levels of Filamin and F-actin to maintain cellular integrity during migration between nurse cells (Sokol & Cooley, 2003; Somogyi & Rørth, 2004). The mediator of these increased F-actin levels, MAL-D, can be activated by Dia (Somogyi & Rørth, 2004). Thus while MMPs may be specific to ECM crossing, a denser and more cross linked actin cortex due to increased levels of the filamin Cheerio and activity of the formin Dia could be a common feature of *Drosophila* cells moving through the resistance of either ECM or surrounding tissues. Determining if such shifts in cell surface actin properties underlie some cancer cells' capacity to metastasize even in the presence of MMP inhibitors is an interesting area of inquiry (Butcher et al 2009; Kessenbrock et al 2010).

Implications for vertebrate immune cell migration

Our work also suggests a new perspective on the migration of some vertebrate immune cells. We find that altering lamin levels does not normally affect *Drosophila* macrophage tissue invasion. This contrasts with results showing that nuclear deformability from lower lamin levels underlies the migration of some immune cell types through narrow constrictions engineered from rigid materials (Davidson et al., 2014; Thiam et al, 2016).

Belyaeva et al

However, negotiation of such extremely challenging *in vitro* environments can lead to DNA damage (Raab et al., 2016) and higher nuclear flexibility caused by lower lamin levels is associated with increased cell death (Harada et al., 2014). A robust cell surface actin layer would allow long-lived cells or those not easily replenished to protect their genome as they move through resistant yet deformable environment. Embryonic *Drosophila* and vertebrate tissue resident macrophages migrate into tissues during development, survive into the adult, and serve as founders of proliferative hematopoietic niches (Holz et al., 2003; Makhijani et al., 2011; Bosch et al., 2019; Ginhoux and Guillems, 2016; Theret et al 2019; Guillems et al, 2020). Tissue resident memory T cells migrate in response to infection in mature animals, are long-lived and not easily renewed from the blood (Szabo et al., 2019). Thus the importance of nuclear mechanics for migration in challenging *in vivo* environments should be explored for a broader range of immune cells as well as the utilization of cortical actin as a strategy for genomic protection.

Materials and Methods

Fly strains and genetics

Flies were raised on standard food bought from IMBA (Vienna, Austria) containing agar, cornmeal, and molasses with the addition of 1.5% Nipagin. Adults were placed in cages in a fly room or a Percival DR36VL incubator maintained at 25°C and 65% humidity or a Sanyo MIR-153 incubator at 29°C within the humidity controlled 25°C fly room; embryos were collected on standard plates prepared in house from apple juice, sugar, agar and Nipagin supplemented with yeast from Lesaffre (Marcq, France) on the plate surface. Fly crosses and embryo collections for RNA interference experiments (7 hour collection) as well as live

Belyaeva et al

imaging (6 hour collection) were conducted at 29°C to optimize expression under GAL4 driver control (Duffy, 2002). All fly lines utilized are listed below.

Fly stocks

srpHemo-GAL4 (mac>) was provided by K. Brückner (UCSF, USA)(Brückner et al., 2004). *Oregon R (control)*, *P{CaryP}attP2 (control)*, *P{CaryP}attP40 (control)*, *kay² (Dfos²)*, *(UAS-Fra)2 (Dfos)*, *UAS-Rho1.N19 Rho1DN*, *UAS-fbz (DfosDN)*, *UAS-kayak RNAi (Dfos RNAi)* TRiP HMS00254 and TRiP JF02804, *UAS-dia RNAi* TRiP HM05027, *UAS-LamC RNAi* TRiP JF01406 and TRiP HMS00308, *e22c-GAL4 (ecto>)*, *Resille::GFP*, *UAS-GFP.nls*, *UAS-mCherry.nls*, *UAS-CD8::GFP* lines were obtained from the Bloomington Stock Center (Indiana, USA). *kay¹ (Dfos¹)* line was provided by O. Schuldiner (WIS, Israel). *UAS-dia.deltaDad.EGFP (diaCA)* and *srpHemo-GAL4 UAS-CLIP::GFP (mac>CLIP::GFP)* lines were provided by B. Stramer (KCL, UK). *UAS-cher.FLAG (cher)* line was provided by M. Uhlirova (CECAD, Germany). *w[1118] (control)*, *UAS-cher RNAi* KK107451, *UAS-TM4SF RNAi* KK102206, *UAS-Lam RNAi¹* GD45636, *UAS-Lam RNAi²* KK107419 lines were obtained from the Vienna *Drosophila* Resource Center (Austria).

Extended genotypes:

Here we list the lines used in each Fig; we state first the name from FlyBase; in parentheses the name used in the Fig panels is provided.

Fig 1 and S1 Fig:

Fig 1D: *Oregon R*. Fig 1E-G and S1A Fig: *srpHemo-GAL4, UAS-GFP (control)*. Fig 1H: *srpHemo-GAL4, UAS-GFP; kay¹ (Dfos¹)*. Fig 1I-L and S1B, G Fig: *srpHemo-GAL4, UAS-GFP.nls/+ (control 1)*. Fig 1H, 1J, 1N: *srpHemo-GAL4, UAS-GFP/+; kay¹ (Dfos¹)*. Fig 1K, 1N and S1B Fig: *srpHemo-GAL4, UAS-GFP.nls/+; kay² (Dfos²)* Fig 1L, 1N: *srpHemo-GAL4, UAS-GFP.nls/(UAS-Fra)2; kay² (Dfos²;mac>Dfos)*. Fig 1O, 1Q and S1C-E Fig: *srpHemo-Gal4,*

Belyaeva et al

584 *srpHemo-H2A::3xmCherry/+* (control 2). Fig 1P-Q and S1C-E Fig: *srpHemo-Gal4, srpHemo-*
585 *H2A::3xmCherry/UAS-fbz* (*mac>DfosDN*). Fig 1R and S1F Fig: *srpHemo-GAL4, UAS-GFP,*
586 *UAS-H2A::RFP/ P{CaryP}attP2* (control). Fig 1R and S1F Fig: *srpHemo-GAL4, UAS-GFP,*
587 *UAS-H2A::RFP /UAS-kayak RNAi HMS00254 and JF02804* (*mac>Dfos RNAi¹, mac>Dfos*
588 *RNAi²*). S1G Fig: *srpHemo-GAL4, UAS-GFP.nls/(UAS-Fra)2* (*mac>Dfos*).

Fig 2 and S2 Fig:

590 Fig 2A, 2C-I and S2A-B, E Fig: *srpHemo-Gal4, srpHemo-H2A::3xmCherry/+* (control). Fig
591 2D: *srpHemo-Gal4, srpHemo-H2A::3xmCherry/+* (3 movies) and *Resille::GFP/+; srpHemo-*
592 *Gal4, srpHemo-H2A::3xmCherry/+* (4 movies, control) and *Resille::GFP/+; srpHemo-Gal4,*
593 *srpHemo-H2A::3xmCherry/+* (3 movies) and *Resille::GFP/+; srpHemo-Gal4, srpHemo-*
594 *H2A::3xmCherry/UAS-DfosDN* (4 movies, *DfosDN*) Fig 2A, 2C-I and S2A-B, E Fig: *srpHemo-*
595 *Gal4, srpHemo-H2A::3xmCherry/UAS-fbz* (*mac>DfosDN*). S2C-D Fig: *srpHemo-GAL4, UAS-*
596 *GFP.nls/+* (control). S2C-D Fig: *srpHemo-GAL4, UAS-GFP.nls/+; kay² (Dfos²)*.

Fig 3 and S3 Fig:

598 Fig 3C, G and S3D Fig: *UASDicer2;; srpHemo-Gal4, srpHemo-H2A::3xmCherry/w¹¹¹⁸*
599 (control). Fig 3D, 3G and S3D Fig: *UASDicer2; UAS-TM4SF RNAi KK10220/+; srpHemo-*
600 *Gal4, srpHemo-H2A::3xmCherry/+* (*mac>TM4SF RNAi*). Fig 3E, G and S3D Fig:
601 *UASDicer2; UAS-cher RNAi KK107451/+; srpHemo-Gal4, srpHemo-H2A::3xmCherry/+*
602 (*mac>cher RNAi*). Fig 3F-G: *UAS-Dicer2;UAS-cher RNAi KK107451/UAS-TM4SF RNAi*
603 *KK102206; srpHemo-Gal4, srpHemo-H2A::3xmCherry/+* (*mac>TM4SF RNAi, cher RNAi*).
604 Fig 3H, L: *srpHemo-GAL4, UAS-mCherry.nls/UAS-mCD8::GFP* (control). Fig 3I, L:
605 *srpHemo-GAL4, UAS-mCherry.nls/UAS-mCD8::GFP; UAS-fbz/+* (*mac>DfosDN*). Fig 3J,
606 L: *srpHemo-GAL4,UAS-mCherry.nls/UAS-cheerio.FLAG; UAS-fbz/+* (*mac>DfosDN, cher*).
607 Fig 3K-L: *srpHemo-GAL4,UAS-mCherry.nls/UAS-TM4SF; UAS-fbz/+* (*mac>DfosDN,*
608 *TM4SF*). Fig 3L: *srpHemo-GAL4, UAS-mCherry.nls/ UAS-TM4SF* (*mac>TM4SF*). Fig 3L:

Belyaeva et al

srpHemo-GAL4, UAS-mCherry.nls/ UAS-cher (mac>cher). S3A-C Fig: *srpHemo-Gal4*,

srpHemo-3xmCherry/+ (control). S3A-C Fig: *srpHemo-Gal4, srpHemo-3xmCherry/UAS-fbz*

(mac>DfosDN).

Fig 4 and S4 Fig:

Fig 4B, D: *srpHemo-Gal4, srpHemo-moe::3xmCherry/+;UAS-mCD8::GFP/+*

(Control). Fig 4C-D: *srpHemo-Gal4, srpHemo-moe::3xmCherry/UAS-fbz (mac>DfosDN)*.

Fig 4E-F: *srpHemo-Gal4, srpHemo-moe::3xmCherry/w118 (Control)*. Fig 4E, G: *srpHemo-*

Gal4, srpHemo-moe::3xmCherry/UAS>cher

RNAi KK107451 (mac>cher RNAi). Fig 4E, H: *srpHemo-Gal4, srpHemo-*

moe::3xmCherry/UAS>TM4SF RNAi KK102206 (mac>TM4SF RNAi). Fig 4I-J: *srpHemo-*

GAL4, UAS-mCherry.nls/UAS-mCD8::GFP (control). Fig 4I', J:

srpHemo-GAL4, UAS-mCherry.nls/UAS-Dia.deltaDad.EGFP; UAS-fbz/+ (mac>

DfosDN, diaCA). Fig 4J: *srpHemo-GAL4, UAS-mCherry.nls/UAS-mCD8::GFP; UAS-fbz/+*

(mac>DfosDN). Fig 4J: *srpHemo-GAL4, UAS-mCherry.nls/ UAS-Dia.deltaDad.EGFP*

(mac>diaCA). Fig 4K-L and S4B-C Fig: *UASDicer2;; srpHemo-Gal4, srpHemo-*

H2A::3xmCherry/P{CaryP}attP40 (control). Fig 4K', L and S4B-C Fig: *UASDicer2;+;*

srpHemo-Gal4, srpHemo-H2A::3xmCherry/ UAS-dia RNAi HM05027 (mac>dia RNAi¹). Fig

4L and S4B-C Fig: *UASDicer2;+; srpHemo-Gal4, srpHemo-H2A::3xmCherry/UAS-dia*

RNAi HMS00308 (mac>dia RNAi²).

Fig 5 and S5 Fig:

Fig 5A and S5A Fig: *srpHemo-Gal4 UAS-LifeActGFP UAS-RedStinger/ srpHemo-Gal4*

UAS-LifeActGFP, UAS-RedStinger control; srpHemo-Gal4 UAS-LifeActGFP UAS-

RedStinger/ srpHemo-Gal4 UAS-LifeActGFP UAS-RedStinger; UAS-DfosDN/UAS-DfosDN.

Fig 5B-D and S5B-D Fig: *srpHemo-Gal4, UAS-CLIP::GFP, UAS-RedStinger (control)*. Fig

5B-D and S5B-D Fig: *srpHemo-Gal4, UAS-CLIP::GFP, UAS-RedStinger; UAS-fbz*

Belyaeva et al

634 (*mac>DfosDN*). Fig 5E, G: *srpHemo-GAL4, UAS-mCherry.nls/UAS-mCD8::GFP (control)*.
 635 Fig 5E'-E'', 5G: *srpHemo-GAL4, UAS-mCherry.nls/UAS-Lamin RNAi* GD45636,
 636 KK107419 (*mac>Lam RNAi¹* and *mac>Lam RNAi²*, respectively). Fig 5E''', G: *srpHemo-*
 637 *GAL4, UAS-mCherry.nls/UAS-LaminC RNAi* TRIP JF01406 (*mac>LamC RNAi*). Fig 5F-G:
 638 *srpHemo-GAL4, UAS-mCherry.nls/UAS-mCD8::GFP; UAS-fbz/+ (mac>DfosDN)*. Fig
 639 5F',F'', G: *srpHemo-GAL4, UAS-mCherry.nls/UAS-Lam RNAi* (*Lam RNAi¹*=GD45636, *Lam*
 640 *RNAi²*=KK107419); *UAS-fbz/+ (mac>DfosDN, Lam RNAi¹* and *mac>DfosDN, Lam RNAi²*).
 641 Fig 5F''', G: *srpHemo-GAL4, UAS-mCherry.nls/UAS-LaminC RNAi* TRIP JF01406; *UAS-*
 642 *fbz/+ (mac>DfosDN, LamC RNAi)*. Fig 5H: *e22CGal4, srpHemo-H2A::3xmCherry/+*
 643 (*control*). Fig 5H: *srpQF/ srpHemo-H2A::3xmCherry; QUAS-fbz/UAS-Rho1.N12*
 644 (*mac<>DfosDN*). Fig 5H: *e22CGal4, srpHemo-H2A::3xmCherry/srpQF; +/- UAS-Rho1.N12*
 645 (*ecto>Rho1DN*). Fig 5H: *srpQF/ e22C-Gal4, srpHemo-H2A::3xmCherry; UAS-*
 646 *Rho1N12/QUAS-fbz (mac<>DfosDN, ecto>rhoDN)*. S5E Fig: +; *UAS-GFP::nls, srpHemo-*
 647 *GAL4 (control)*. +; *UAS-GFP::Lamin, srpHemo-GAL4*.

648

649 **Cloning and generation of QUAS-DfosDN line**

650 The fragment was amplified from genomic DNA of the published *UAS-fbz (UAS-Dfos DN)*
 651 line (Eresh, Riese, Jackson, Bohmann, & Bienz, 1997) using primers encompassing a 5'
 652 consensus translation initiation sequence followed by the bZIP fragment and containing
 653 BglIII and XhoI restriction sites: 5'-GAAGATCTATTGGGAATTCAACATGACCCCG-3'
 654 and 5'-CCCTCGAGTCAGGTGACCACGCTCAGCAT-3'. The resulting fragment was
 655 cloned into the pQUAS vector, a gift from Christopher Potter (Addgene plasmid # 104880).
 656 The final construct was sequenced and injected into the attP2 landing site by BestGene
 657 (Chino Hills, CA, USA).

658

Belyaeva et al

Cloning and generation of UAS-TM4SF line

The TM4SF open reading frame was amplified from the DGRC GH07902 cDNA clone (#3260, Fbcl0121651), using primers acagcgGAATTCATGGCATTGCCGAAGAAAAT and acagcgTCTAGATTAAAAGCTAATCGTCTGTCATT. The PCR product and the pUAS⁺-aTTB vector (DGRC plasmid #1419) were digested with EcoRI and XbaI, and ligated. After sequencing, the construct was injected into the landing site line, (*y¹ M{vas-int.Dm}ZH-2A w^{*}; M{3xP3-RFP.attP}ZH-51D*, BL 24483), to produce second chromosome inserts. All male survivors were crossed to *w; Sp/CyO; PrDr/TM3Ser* virgins. Transformants were recognized by eye color and crossed again to *w; Sp/CyO; PrDr/TM3Ser* virgins to get rid of the X chromosomal integrase.

Embryo staging:

Laterally oriented embryos with complete germband (gb) extension and the presence of stomadeal invagination were staged based on gb retraction from the anterior as a percentage of total embryo length. Embryos with no gb retraction were classified as Stage 11, 30% retraction early Stage 12, 60% retraction Stage 12, and 70% Stage 13. Imaged embryos are shown throughout paper in a lateral orientation with anterior to the left and dorsal up.

In situ hybridization and immunofluorescence

Embryos were fixed with 3.7% formaldehyde/heptane for 20 min followed by methanol devitellinization for *in situ* hybridization and visualization of 3xmCherry. The *Dfos* cDNA clone SD04477 was obtained from the DGRC. T7 or T3 polymerase-synthesized digoxigenin-labelled anti-sense probe preparation and *in situ* hybridization was performed using standard methods (Lehmann & Tautz, 1994). Images were taken with a Nikon-Eclipse Wide field microscope with a 20X 0.5 NA DIC water Immersion Objective. Embryos were

Belyaeva et al

mounted after immunolabeling in Vectashield Mounting Medium (Vector Labs, Burlingame, USA) and imaged with a Zeiss Inverted LSM700 and LSM800 Confocal Microscope using a Plain-Apochromat 20X/0.8 Air Objective or a Plain-Apochromat 63X/1.4 Oil Objective as required.

Antibody	Source animal	Dilution	Provided by
Anti-Dfos	Rabbit	1:50	J. Zeitlinger (Stowers Institute, USA)
Anti-GFP	Chicken	1:500	Abcam (ab13970)
Anti-mCherry	Goat	1:200	Invitrogen (M11217)

Dfos antibody

The Dfos rabbit polyclonal antibody was produced for the lab of Julia Zeitlinger. It was raised by Genescript (Piscataway, NJ, USA) against the C-terminal end of *Drosophila* Kayak found in all isoforms and was purified against an N terminally His tagged antigen corresponding to aa 73 to 595 of Kay isoform A. The internal Genescript order number is 163185-30, and in the Zeitlinger lab is referred to as anti-kay/fos Ab.

Time-Lapse Imaging

Embryos were dechorionated in 50% bleach for 5 min, washed with water, and mounted in halocarbon oil 27 (Sigma) on a 24x50mm high precision coverslip (Marienfeld Laboratory Glassware, No. 1.5H) between two bridges (~0.5 cm high) of coverslips glued on top of each other, or mounted in halocarbon oil 27 (Sigma) between a 18x18mm coverslip (Marienfeld Laboratory Glassware, No. 1.5H) and an oxygen permeable membrane (YSI). The embryo was imaged on an upright multiphoton microscope (TrimScope, LaVision) equipped with a W Plan-Apochromat 40X/1.4 oil immersion objective (Olympus). GFP and mCherry were imaged at 860 nm and 1100 nm excitation wavelengths, respectively, using a Ti-Sapphire femtosecond laser system (Coherent Chameleon Ultra) combined with optical parametric oscillator technology (Coherent Chameleon Compact OPO). Excitation intensity

Belyaeva et al

profiles were adjusted to tissue penetration depth and Z-sectioning for imaging was set at 1µm for tracking. For long-term imaging, movies were acquired for 60 - 150 minutes with a frame rate of 25-45 seconds. A temperature control unit set to 29°C was utilized for all genotypes except *kay*² for which the setting was 25°C.

Image Analysis

Macrophage cell counts: Autofluorescence of the embryo revealed the position of the germband (gb) for staging of fixed samples. Embryos with 40% (±5%) gb retraction (Stage 12) were analysed for macrophage numbers in the pre-gb, within the germband, along the ventral nerve cord (vnc) and in the whole embryo. For the *kay RNAi* embryos with 70% gb retraction (Stage 13) were used for vnc counts. The pre-gb zone was defined based on embryo and yolk autofluorescence as an area on the yolk sac underneath the amnioserosa with borders defined posteriorly by the gb ectoderm and anteriorly by the head. Macrophages were visualized using confocal microscopy with a Z-stack step size of 2 µm and macrophage numbers within the gb or the segments of the vnc were calculated in individual slices (and then aggregated) using the Cell Counter plugin in FIJI. Total macrophage numbers were obtained using Imaris (Bitplane) by detecting all the macrophage nuclei as spots.

Macrophage Tracking, Speed, Persistence. Mode of Migration and Macrophage gb crossing Analysis

Embryos with macrophage nuclei labelled with *srpHemo-H2A::3XmCherry* and the surrounding tissues with *Resille::GFP*, or with only macrophages labelled by *srpHemo-H2A::3XmCherry*, or *srpHemo>GFP.nls* were imaged and 250x250x40µm³ 3D-stacks were typically acquired with ~0.2x0.2x1µm³ voxel size every 39-41 seconds for ~2 hours. For

Belyaeva et al

imaging macrophages on vnc frames were acquired at every 40-43 seconds for 30 min after macrophages started spreading into abdominal segment 2 (see Fig 2G). Multiphoton microscopy images were initially processed with ImSpector software (LaVision Bio Tec) to compile channels, and exported files were further processed using Imaris software (Bitplane) for 3D visualization.

Each movie was rotated and aligned along the embryonic AP axis for tracking analysis. For analysis of migration in the pre-gb and gb in the control and *kay*² mutant, embryos were synchronized using the onset of germ and retraction. For vnc migration analysis, macrophages were tracked for 30 minutes from when macrophages started moving into the second abdominal segment. Only macrophages migrating along the inner edge of the vnc were analyzed.

Gb crossing time was calculated from when the macrophages align in front of the gb ectoderm in a characteristic arc, until the first macrophage had transitioned its nucleus inside the ecto-meso-interphase. To see the gb edge and yolk in movies of *srpHemo-3xH2A::mCherry*, either *Resille::GFP* labelling the outlines of all cells, or the auto-fluorescence of the yolk was used.

For analysis of gb migration in the *DfosDN* vs control macrophages, macrophages were tracked from when the first macrophage appeared between the ectoderm and the yolk sac until gb retraction started, typically 60 minutes. In the head and pre-gb, macrophage nuclei were extracted using the spot detection function, and tracks generated in 3D over time. The pre-gb and gb were defined as for macrophage counts described above. The mean position of the tracks in X- and Y restrict analysis to each migratory zones.

Cell speed and persistence were calculated from nuclei positions using custom Python scripts as described elsewhere (Smutny et al., 2017). Briefly, instantaneous velocities from single cell trajectories were averaged to obtain a mean instantaneous velocity value over the

Belyaeva et al

course of measurement. The directional persistence of a trajectory was calculated as the mean cosine of an angle between subsequent instantaneous velocities:

$$I(v_1, \dots, v_l) = \frac{1}{l-1} \sum_{k=1}^{l-1} \cos(v_k, v_{k+1}),$$

where l is duration of the trajectory and v_1, \dots, v_l are its instantaneous velocities. Only trajectories with a minimal duration of 15 timeframes were used. Calculated persistence values were averaged over all trajectories to obtain a persistence index (I) for the duration of measurement (with -1 being the lowest and 1 the maximum). 3-6 embryos were recorded and analyzed for each genotype, numbers of control and perturbed embryos are equal in each pairwise comparison.

Measurement of junctional Phalloidin

The junctional intensity of F-actin (Phalloidin) was calculated using linescan analysis as previously described (Smutny et al., 2010) with the following changes. The line was ~5 μm and was always drawn in the middle slice of the Z stack (1 μm resolution) of the macrophage-macrophage junction. For every line, a Gaussian fit was applied and maximum intensities across the cell junction were then normalized against average intensities of F-actin (Phalloidin) staining in the stereotypical gb area of ~50x50 μm² in each embryo. Analyses were carried out using standard Fiji software. 4-5 embryos were analysed per genotype. Macrophages in the pre-gb or gb entry zones were analyzed.

Measurement of F-actin reporters

To quantify cortical F-actin intensity in living embryos, a *srpHemo-moe::3xmCherry* reporter line (Gyoergy et al., 2018) was crossed into a background of macrophages expressing *DfosDN*, *cher RNAi*, or *TM4SF RNAi*. Embryos were collected for 5h 30min at

Belyaeva et al

29°C, de-chorionated in 50% bleach for 5 min, rinsed thoroughly with water, and aligned laterally side by side under a stereomicroscope using a fluorescence lamp to check for the presence of mCherry. Aligned embryos were then mounted as described in the live imaging section above. To image Moe::3xmCherry, a Zeiss LSM800 inverted microscope was used with the following settings: Plan-APOCHROMAT 40x/1.4 Oil, DIC, WD=0.13 objective, 1.5x zoom, 1025x1025 pixel, speed 8, heating chamber set to 29°C, z-interval 1µm. Laser settings were kept constant in all experiments. Images were acquired during macrophage invasion into the gb (St 12). Pseudo-coloring was conducted for the mCherry red channel. Each pixel in the image has a color ascribed to it via the fire “Look Up Table” translating the level of intensity of the mCherry channel into a defined amount of each color. The highest intensity of the image is represented as very bright yellow and all other grey values are depicted as colors on the scale accordingly.

For quantification of Moe::3xmCherry intensity, an ROI was drawn in Fiji software around macrophages at the germband entry site in 20 z-stacks for each embryo. The area mean intensity was measured in all ROIs and the average/embryo was calculated. To normalize fluorescence intensities per batch, the average intensity/embryo of all ROIs in each sample was divided by the arithmetic mean of the average intensity/embryo of all ROIs in the control per batch. The normalized average intensities/embryo were then compared to each other using a t-test with Welch’s correction for *DfosDN* and one way-ANOVA for *cher RNAi* and *TM4SF RNAi*.

Cell aspect ratio analysis and imaging actin dynamics

Laterally oriented embryos were used to measure the maximal length and width of macrophages expressing *UAS-CLIP::GFP* under the control of *srpHemoGal4*. Briefly, 3D-stacks with 1 µm Z resolution were acquired every 35-45 seconds for approximately 1 hour. As the strength of the GAL4 expression increased over time, laser power was adjusted

Belyaeva et al

during acquisition to reach the best possible quality of visualization. Images acquired from mutiphoton microscopy were initially processed with ImSpector software (LaVision Bio Tec) to compile channels from the imaging data. We started measuring from the time the cell body of the first macrophage fully appeared at the interface between the ectoderm and mesoderm and yolk sac until it had moved 30 μm along the ectoderm mesoderm interface. At each timeframe, a line was drawn in Fiji along the longest dimension of the macrophage in the direction of its front-rear polarization axis, denoted the maximal cell length, and along the orthologonal longest dimension, which was considered maximal cell width. We did not observe long CLIP::GFP protrusions, but when a small protrusion was present, it was not included in the length measurement; within this gb region the front of the first macrophage was clearly outlined with CLIP::GFP. The border between the first and second entering macrophages was drawn based on the uninterrupted intense line of CLIP::GFP at the base of the first macrophage; only cells with a clearly visible border were measured. The length to width ratio was quantified for each timeframe and a probability density function was plotted: 5 embryos were recorded for each genotype.

Imaging the actin protrusion

Laterally oriented embryos expressing *srpHemo-Gal4 UAS-LifeAct::GFP* were used to image macrophage actin live with a 3D-stack resolution of 1 μm . See above description of CLIP::GFP labeled macrophage imaging for laser power and image compilation. Laser power was also increased further in the DfosDN samples to enhance actin visualization. We measured the length of the filopodia-like protrusion of the first entering macrophage with Imaris software (Bitplane) from the time when the protrusion was inserted into the ectoderm, mesoderm and yolk sac interface until the macrophage started to translocate its cell body into that location.

Belyaeva et al

FACS sorting of macrophages

Adult flies of either *w;+;srpHemoGal4,srpHemo::3xmCherry/+* or *w;+;srpHemoGal4,srpHemo::3xmCherry/UASDfosDN* genotypes were placed into plastic cages closed with apple juice plates with applied yeast to enhance egg laying. Collections were performed at 29°C for 1 hour, then kept at 29°C for additional 5 hours 15 minutes to reach stage 11-early stage 12. Embryos were harvested for 2 days with 6-7 collections per day and stored meanwhile at +4°C to slow down development. Collected embryos were dissociated and the macrophages sorted as previously described (Gyoergy et al., 2018). About $1-1.5 \times 10^5$ macrophages were sorted within 30 minutes.

Sequencing of the macrophage transcriptome

Total RNA was isolated from FACS-sorted macrophages using Qiagen RNeasy Mini kit (Cat No. 74104). The quality and concentration of RNA was determined using Agilent 6000 Pico kit (Cat No. 5067-1513) on an Agilent 2100 Bioanalyzer: on average about 100 ng of total RNA was extracted from 1.5×10^5 macrophages. RNA sequencing was performed by the CSF facility of Vienna Biocenter according to standard procedures (<https://www.vbcf.ac.at/facilities/next-generation-sequencing/>) on three replicates. Briefly, the cDNA library was synthesized using QuantSeq 3' mRNA-seq Library Prep kit and sequenced on the Illumina HiSeq 2500 platform. The reads were mapped to the *Drosophila melanogaster* Ensembl BDGP6 reference genome with STAR (version 2.5.1b) The read counts for each gene were detected using HTSeq (version 0.5.4p3). The Flybase annotation (r6.19) was used in both mapping and read counting. Counts were normalised to arbitrary units using the TMM normalization from edgeR package in R. Prior to statistical testing the data was voom transformed and then the differential expression between the sample groups

Belyaeva et al

was calculated with limma package in R. The functional analyses were done using the topGO and gage packages in R (Anders, Pyl, & Huber, 2015; Dobin et al., 2013).

Primer	Sequence
Fos_fw	ATGGTGAAGACCGTGTTCAGG
Fos_rv	GTTGATCTGTCTCCGCTTGGA
Flna_fw	GTCACAGTGTCAATCGGAGGT
Flna_rv	TTGCCTGCTGCTTTTGTGTC
Flnb_fw	TTCTACACTGCTGCCAAGCC
Flnb_rv	CTGTAACCCAGGGCCTGAATC
Flnc_fw	CATCACCCGGAGTCCTTTCC
Flnc_rv	CTCTGTGCCCTTTGGACCTT
Tspan6_fw	TCGAAGTAGTTGCCGCCATT
Tspan6_rv	CCGCAACAATGCAACGTACT
Gstt3_fw	GGAGCTCTACCTGGACCTGA
Gstt3_rv	AAGATGGCCACACTCTCTGC
Evalc_fw	GTTGCCTACGCATGTGTTCC
Evalc_rv	CCGATGCAGACACTGGACAT
Tspo_fw	GTATTCAGCCATGGGGTATGG
Tspo_rv	AAGCAGAAGATCGGCCAAGG
Tbp_fw	GGGGAGCTGTGATGTGAAGT
Tbp_rv	CCAGGAAATAATTCTGGCTCAT

qRT-PCR analysis of mRNA levels in murine bones and osteosarcomas

RNA isolation and qPCR was performed from bones of wild-type C57BL/6 mice and from bones and osteosarcomas (OS) of H2-c-fosLTR as previously described with the above primers (Rüther et al., 1989).

Statistical and Repeatability

Mouse experiments:

Data are shown as mean \pm SEM. One-way ANOVA followed by Tukey's multiple comparisons post-test was applied to compare experimental groups. Statistical analysis was performed using GraphPad Prism 6.0 software. A p-value <0.05 was considered statistically significant (*p<0.05, **p<0.01, ***p<0.001, ****p<0.0001).

Drosophila experiments:

Belyaeva et al

Statistical tests as well as the number of embryos/cells/tracks/contacts assessed are listed in the Figure legends. All statistical analyses were performed using GraphPad PRISM or R Studio and significance was determined using a 95% confidence interval. No statistical method was used to predetermine sample size. An unpaired t-test and Mann-Whitney U Test were used to calculate the significance in differences between two groups and One-Way ANOVA followed by Tukey HSD post hoc test was used for multiple comparisons.

Representative images of Dfos antibody staining were analyzed per replicate per genotype and *in situ* hybridization are from experiments that were repeated 2 times with many embryos with reproducible results. Representative images and plots of different *Dfos* mutants in Fig 1 and S1 Fig are from experiments that were repeated 2-3 times. In live imaging experiments in Fig 2 and S2 Fig, 3-7 embryos for each genotype were analyzed, each embryo was recorded in a separate day. Three replicates were conducted of FACS sorting macrophages from embryos, and then preparing RNA samples for RNA sequencing for each genotype. Representative images and plots of RNAi and rescue experiments in Fig 4 and S4 Fig are from experiments that were repeated 2-3 times. Representative images and plots of phalloidin immunostaining in Fig 4 are from experiments that were repeated 4 times. For all immunostaining experiments 3-7 embryos were analyzed per replicate per genotype. In Moe::3xmCherry experiments in Fig 4D, 11 and 12 embryos were analysed for the control and *DfosDN*, and in Fig 4E 10, 8, and 8 embryos were analysed for the control, *cher RNAi*, and *TM4SF RNAi* respectively, as indicated in the graph and in the relevant part of the F-actin reporter measurement section of the methods. In the LifeAct::GFP protrusion live imaging experiment in Fig 5 and S5 Fig, 3-5 embryos were analyzed for each genotype. In CLIP::GFP live imaging experiments in Fig 5 and S5 Fig, 5-6 embryos were analyzed for each genotype for the cell aspect ratio in germband zone, and 2 embryos in pre-germband zone and for tracking of the front vs rear speed. Each embryo was recorded on a separate

Belyaeva et al

day. The Lamin over expression in S5 Fig and the Lamin knockdown rescue experiments in Fig 5G were repeated at least 3 times with reproducible results. Gb rescue experiment in Fig 5H was repeated at least 4 times with reproducible results.

Acknowledgements

We thank the following for their contributions: The *Drosophila* Genomics Resource Center supported by NIH grant 2P40OD010949-10A1 for plasmids, K. Brueckner, B. Stramer, M. Uhlirova, O. Schuldiner, the Bloomington *Drosophila* Stock Center supported by NIH grant P40OD018537 and the Vienna *Drosophila* Resource Center for fly stocks, FlyBase (Thurmond et al., 2019) for essential genomic information, and the BDGP *in situ* database for data (Tomancak et al., 2002, 2007). For antibodies, we thank the Developmental Studies Hybridoma Bank, which was created by the Eunice Kennedy Shriver National Institute of Child Health and Human Development of the NIH, and is maintained at the University of Iowa, as well as J. Zeitlinger for her generous gift of Dfos antibody. We thank the Vienna BioCenter Core Facilities for RNA sequencing and analysis and the Life Scientific Service Units at IST Austria for technical support and assistance with microscopy and FACS analysis. We thank C.P. Heisenberg, P. Martin, M. Sixt and Siekhaus group members for discussions and T.Hurd, A. Ratheesh and P. Rangan for comments on the manuscript. A.G. was supported by the Austrian Science Fund (FWF) grant DASI_FWF01_P29638S, D.E.S. by Marie Curie CIG 334077/IRTIM. M.S. is supported by the FWF, PhD program W1212 and the European Research Council (ERC) Advanced grant (ERC-2015-AdG TNT-Tumors 694883). S.W. is supported by an OEAW, DOC fellowship.

References

- Anders, S., Pyl, P. T., & Huber, W. (2015). HTSeq-A Python framework to work with high-throughput sequencing data. *Bioinformatics*, 31(2), 166–169. <https://doi.org/10.1093/bioinformatics/btu638>
- Andrés, V., & González, J. M. (2009). Role of A-type lamins in signaling, transcription, and chromatin organization. *Journal of Cell Biology*, 187(7), 945–957. <https://doi.org/10.1083/jcb.200904124>
- Bellanger, J. M., Astier, C., Sardet, C., Ohta, Y., Stossel, T. P., & Debant, A. (2000). The Rac1- and RhoG-specific GEF domain of trio targets filamin to remodel cytoskeletal actin. *Nature Cell Biology*, 2(12), 888–892. <https://doi.org/10.1038/35046533>
- Benhra, N., Barrio, L., Muzzopappa, M., & Milán, M. (2018). Chromosomal Instability Induces Cellular Invasion in Epithelial Tissues. *Developmental Cell*, 47(2), 161-174.e4. <https://doi.org/10.1016/j.devcel.2018.08.021>
- Berditchevski, F., & Odintsova, E. (1999). Characterization of integrin-tetraspanin adhesion complexes: Role of tetraspanins in integrin signaling. *Journal of Cell Biology*, 146(2), 477–492. <https://doi.org/10.1083/jcb.146.2.477>
- Bershadsky, A. D., Balaban, N. Q., & Geiger, B. (2003). Adhesion-Dependent Cell Mechanosensitivity. *Annual Review of Cell and Developmental Biology*, 19(1), 677–695. <https://doi.org/10.1146/annurev.cellbio.19.111301.153011>
- Bilancia, C. G., Winkelman, J. D., Tsygankov, D., Nowotarski, S. H., Sees, J. A., Comber, K., ... Peifer, M. (2014). Enabled negatively regulates diaphanous-driven actin dynamics in vitro and in vivo. *Developmental Cell*, 28(4), 394–408. <https://doi.org/10.1016/j.devcel.2014.01.015>
- Bosch, P.S., Makhijani, K., Herboso, L., Gold, K.S., Baginsky, R., Woodcock, K.J., Alexander, B., Kukar, K., Corcoran, S., Jacobs, T., Ouyang, D., Wong, C., Ramond, E.J.V., Rhiner, C., Moreno, E., Lemaitre, B., Geissmann, F., & Brueckner, K. (2019). Adult *Drosophila* lack hematopoiesis but rely on a blood cell reservoir at the respiratory epithelia to relay infection signals to surrounding tissues. *Developmental Cell*, 51(6)787-803. <https://doi.org/10.1016/j.devcel.2019.10.017>
- Brock, A. R., Wang, Y., Berger, S., Renkawitz-Pohl, R., Han, V. C., Wu, Y., & Galko, M. J. (2012). Transcriptional regulation of profilin during wound closure in *Drosophila* larvae. *Journal of Cell Science*, 125(23), 5667–5676. <https://doi.org/10.1242/jcs.107490>
- Brückner, K., Kockel, L., Duchek, P., Luque, C. M., Rørth, P., & Perrimon, N. (2004). The PDGF/VEGF

Belyaeva et al

- 947 receptor controls blood cell survival in *Drosophila*. *Developmental Cell*, 7(1), 73–84.
- 948 <https://doi.org/10.1016/j.devcel.2004.06.007>
- 949 Brzozowski, J. S., Bond, D. R., Jankowski, H., Goldie, B. J., Burchell, R., Naudin, C., ... Weidenhofer, J.
- 950 (2018). Extracellular vesicles with altered tetraspanin CD9 and CD151 levels confer increased prostate
- 951 cell motility and invasion. *Scientific Reports*, 8(1). <https://doi.org/10.1038/s41598-018-27180-z>
- 952 Butcher, D.T., Alliston, T. & Weaver, V.M.(2009). A tense situation: forcing tumour progression. *Nature*
- 953 *Reviews Cancer*, 9(2), 108-22. . <https://doi.org/10.11038/nrc2544>
- 954 Cho, N. K., Keyes, L., Johnson, E., Heller, J., Ryner, L., Karim, F., & Krasnow, M. A. (2002). Developmental
- 955 control of blood cell migration by the *Drosophila* VEGF pathway. *Cell*, 108(6).
- 956 [https://doi.org/10.1016/S0092-8674\(02\)00676-1](https://doi.org/10.1016/S0092-8674(02)00676-1)
- 957 Chugh, P., Clark, A. G., Smith, M. B., Cassani, D. A. D., Dierkes, K., Ragab, A., ... Paluch, E. K. (2017). Actin
- 958 cortex architecture regulates cell surface tension. *Nature Cell Biology*, 19(6), 689–697.
- 959 <https://doi.org/10.1038/ncb3525>
- 960 Danuser, G., Allard, J., & Mogilner, A. (2013). Mathematical Modeling of Eukaryotic Cell Migration: Insights
- 961 Beyond Experiments. *Annual Review of Cell and Developmental Biology*, 29(1).
- 962 <https://doi.org/10.1146/annurev-cellbio-101512-122308>
- 963 Davidson, A. J., Millard, T. H., Evans, I. R., & Wood, W. (2019). Ena orchestrates remodelling within the actin
- 964 cytoskeleton to drive robust *Drosophila* macrophage chemotaxis. *Journal of Cell Science*, 132(5).
- 965 <https://doi.org/10.1242/jcs.224618>
- 966 Davidson, P.M., Denais, C., Bakshi, M., & Lammerding, J. (2014).. Nuclear deformability constitutes a rate-
- 967 limiting step during cell migration in 3-D environments. *Cellular and Molecular Bioengineering*,
- 968 7(3)293-306. <https://doi.org/10.1007/s12195-014-0342-y>
- 969 Davis, J. R., Luchici, A., Miodownik, M., Stramer, B. M., Davis, J. R., Luchici, A., ... Stramer, B. M. (2015).
- 970 Inter-Cellular Forces Orchestrate Contact Inhibition of Locomotion Article Inter-Cellular Forces
- 971 Orchestrate Contact Inhibition of Locomotion. *Cell*, 161(2), 361–373.
- 972 <https://doi.org/10.1016/j.cell.2015.02.015>
- 973 Delaguillaumie, A., Lagaudrière-Gesbert, C., Popoff, M. R., & Conjeaud H., H. (2002). Rho GTPase link
- 974 cytoskeletal rearrangements and activation processes induced via the tetraspanin CD82 in T lymphocytes.
- 975 *Journal of Cell Science*, 115(2).
- 976 Deluca, T. F., Cui, J., Jung, J. Y., St. Gabriel, K. C., & Wall, D. P. (2012). Roundup 2.0: Enabling comparative

Belyaeva et al

977 genomics for over 1800 genomes. *Bioinformatics*, 28(5). <https://doi.org/10.1093/bioinformatics/bts006>

978 Dobin, A., Davis, C. A., Schlesinger, F., Drenkow, J., Zaleski, C., Jha, S., ... Gingeras, T. R. (2013). STAR:

979 Ultrafast universal RNA-seq aligner. *Bioinformatics*, 29(1), 15–21.

980 <https://doi.org/10.1093/bioinformatics/bts635>

981 Duffy, J. B. (2002). GAL4 system in Drosophila: A fly geneticist's Swiss army knife. *Genesis*, 34(1–2), 1–15.

982 <https://doi.org/10.1002/gene.10150>

983 Edwards, K. A., Demsky, M., Montague, R. A., Weymouth, N., & Kiehart, D. P. (1997). GFP-moesin

984 illuminates actin cytoskeleton dynamics in living tissue and demonstrates cell shape changes during

985 morphogenesis in Drosophila. *Developmental Biology*, 191(1). <https://doi.org/10.1006/dbio.1997.8707>

986 Ehrlicher, A. J., Nakamura, F., Hartwig, J. H., Weitz, D. A., & Stossel, T. P. (2011). Mechanical strain in actin

987 networks regulates FilGAP and integrin binding to filamin A. *Nature*, 478(7368), 260–263.

988 <https://doi.org/10.1038/nature10430>

989 Eresh, S., Riese, J., Jackson, D. B., Bohmann, D., & Bienz, M. (1997). A CREB-binding site as a target for

990 decapentaplegic signalling during Drosophila endoderm induction. *EMBO Journal*, 16(8), 2014–2022.

991 <https://doi.org/10.1093/emboj/16.8.2014>

992 Evans, I. R., & Wood, W. (2011). Drosophila embryonic hemocytes. *Current Biology*, 21(5), R173–R174.

993 <https://doi.org/10.1016/j.cub.2011.01.061>

994 Franck, Z., Gary, R., & Bretscher, A. (1993). Moesin, like ezrin, colocalizes with actin in the cortical

995 cytoskeleton in cultured cells, but its expression is more variable. *Journal of Cell Science*, 105(1).

996 Fujita, M., Mitsuhashi, H., Isogai, S., Nakata, T., Kawakami, A., Nonaka, I., ... Kudo, A. (2012). Filamin C

997 plays an essential role in the maintenance of the structural integrity of cardiac and skeletal muscles,

998 revealed by the medaka mutant zacro. *Developmental Biology*, 361(1), 79–89.

999 <https://doi.org/10.1016/j.ydbio.2011.10.008>

1000 García-Echeverría, C. Methionine-containing zipper peptides. *Lett Pept Sci* 4, 135–140 (1997).

1001 <https://doi.org/10.1007/BF02443525>

1002 Ginhoux, F. & Guillems, M. (2016). Tissue-resident macrophage ontogeny and homeostasis. *Immunity* 44(3),

1003 439–449. <https://doi.org/10.1016/j.immuni.2016.02.024>

1004 Glogauer, M., Arora, P., Chou, D., Janmey, P. A., Downey, G. P., & McCulloch, C. A. G. (1998). The role of

1005 actin-binding protein 280 in integrin-dependent mechanoprotection. *Journal of Biological Chemistry*,

1006 273(3), 1689–1698. <https://doi.org/10.1074/jbc.273.3.1689>

Belyaeva et al

- 1007 Glover, J.N.M. and Harrison, S.C. (1005). Crystal structure of the heterodimeric bZIP transcription factor c-Fos-
1008 c-Jun bound to DNA. *Nature*, 373(6511):257-261. <https://doi.org/10.1038/373257a0>
- 1009 Goldmann, W. H., Tempel, M., Sprenger, I., Isenberg, G., & Ezzell, R. M. (1997). Viscoelasticity of actin-
1010 gelsolin networks in the presence of filamin. *European Journal of Biochemistry*, 246(2), 373–379.
1011 <https://doi.org/10.1111/j.1432-1033.1997.00373.x>
- 1012 Gonzalez-Gaitan, M. & Peifer, M. (2009) Exploring the roles of Diaphanous and Enabled activity in shaping the
1013 balance between filopodia and lamellipodia. *Molecular Biology of the Cell* 20(24).
1014 <https://doi.org/10.1091/mbc.e09-02-0144>
- 1015 Greten, F.R. & Grovannikov, S.I. (2019). Inflammation and Cancer: Triggers, Mechanisms and Consequences.
1016 *Immunity* 51(1), 27-41. <https://doi.org/10.1016/j.immuni.2019.06.025>
- 1017 Großhans, J., Wenzl, C., Herz, H. M., Bartoszewski, S., Schnorrer, F., Vogt, N., ... Müller, H. A. (2005).
1018 RhoGEF2 and the formin Dia control the formation of the furrow canal by directed actin assembly during
1019 Drosophila cellularisation. *Development*, 132(5), 1009–1020. <https://doi.org/10.1242/dev.01669>
- 1020 Guilliams, M., Thierry, G.R., Bonnardel, J., & Bajenoff, M. (2020). Establishment and Maintenance of the
1021 Macrophage Niche. *Immunity* 52(3), 434-451. <https://doi.org/10.1016/j.immuni.2020.02.015>
- 1022 Gyoergy, A., Roblek, M., Ratheesh, A., Valoskova, K., Belyaeva, V., Wachner, S., ... Siekhaus, D. E. (2018).
1023 Tools allowing independent visualization and genetic manipulation of Drosophila melanogaster
1024 macrophages and surrounding tissues. *G3: Genes, Genomes, Genetics*, 8(3).
1025 <https://doi.org/10.1534/g3.117.300452>
- 1026 Hammonds, A. A. S., Bristow, C. C. a, Fisher, W. W., Weiszmann, R., Wu, S., Hartenstein, V., ... Celniker, S.
1027 E. (2013). Spatial expression of transcription factors in Drosophila embryonic organ development.
1028 *Genome Biology*, 14(12), R140. <https://doi.org/10.1186/gb-2013-14-12-r140>
- 1029 Harada, T., Swift, J., Irianto, J., Shin, J, Spinler, K.R., Athirasala, A., Diegmiller, R., Dingal, P.C.D.P.,
1030 Ivanovska, I.L., & Discher, D.E. (2014). Nuclear lamin stiffness is a barrier to 3D migration, but softness
1031 can limit survival. *J. Cell Biology*, 2014(5)669-82. <https://doi.org/10.1083/jcb.201308029>.
- 1032 Heer, N. C., & Martin, A. C. (2017). Tension, contraction and tissue morphogenesis. *Development (Cambridge)*,
1033 144(23). <https://doi.org/10.1242/dev.151282>
- 1034 Holz, A., Bossinger, B., Strasser, T., Janning, W., & Klapper, R. (2003). The two origins of hemocytes in
1035 *Drosophila*. *Development*, 130(20), 4955-62. <https://doi.org/10.1242/dev.007202>
- 1036 Hong, I. K., Jeoung, D. Il, Ha, K. S., Kim, Y. M., & Lee, H. (2012). Tetraspanin CD151 stimulates adhesion-

Belyaeva et al

- 1037 dependent activation of Ras, Rac, and Cdc42 by facilitating molecular association between $\beta 1$ integrins
- 1038 and small GTPases. *Journal of Biological Chemistry*, 287(38), 32027–32039.
- 1039 <https://doi.org/10.1074/jbc.M111.314443>
- 1040 Hu, J., Lu, J., Lian, G., Ferland, R. J., Dettenhofer, M., & Sheen, V. L. (2014). Formin 1 and filamin B
- 1041 physically interact to coordinate chondrocyte proliferation and differentiation in the growth plate. *Human*
- 1042 *Molecular Genetics*, 23(17), 4663–4673. <https://doi.org/10.1093/hmg/ddu186>
- 1043 Kasza, K. E., Broedersz, C. P., Koenderink, G. H., Lin, Y. C., Messner, W., Millman, E. A., ... Weitz, D. A.
- 1044 (2010). Actin filament length tunes elasticity of flexibly cross-linked actin networks. *Biophysical Journal*,
- 1045 99(4), 1091–1100. <https://doi.org/10.1016/j.bpj.2010.06.025>
- 1046 Kessenbrock, K., Plaks, V., & Werb, Z. (2010). Matrix metalloproteinases: regulators of the tumor
- 1047 microenvironment. *Cell* 141(1), 52-67. <https://doi.org/10.1016/j.cell.2010.03.015>
- 1048 Kühn, S., & Geyer, M. (2014). Formins as effector proteins of rho GTPases. *Small GTPases*, 5(JUNE).
- 1049 <https://doi.org/10.4161/sgtp.29513>
- 1050 Külshammer, E., Mundorf, J., Kilinc, M., Frommolt, P., Wagle, P., & Uhlirova, M. (2015). Interplay among
- 1051 Drosophila transcription factors Ets21c, Fos and Ftz-F1 drives JNK-mediated tumor malignancy. *DMM*
- 1052 *Disease Models and Mechanisms*, 8(10), 1279–1293. <https://doi.org/10.1242/dmm.020719>
- 1053 Külshammer, E., & Uhlirova, M. (2013). The actin cross-linker Filamin/Cheerio mediates tumor malignancy
- 1054 downstream of JNK signaling. *Journal of Cell Science*, 126(4), 927–938.
- 1055 <https://doi.org/10.1242/jcs.114462>
- 1056 Kumar, A., Shutova, M. S., Tanaka, K., Iwamoto, D. V., Calderwood, D. A., Svitkina, T. M., & Schwartz, M.
- 1057 A. (2019). Filamin A mediates isotropic distribution of applied force across the actin network. *Journal of*
- 1058 *Cell Biology*, 218(8), 2481–2491. <https://doi.org/10.1083/jcb.201901086>
- 1059 Lehmann, R., & Tautz, D. (1994). In Situ Hybridization to RNA. *Methods in Cell Biology*, 44(C), 575–596.
- 1060 [https://doi.org/10.1016/S0091-679X\(08\)60933-4](https://doi.org/10.1016/S0091-679X(08)60933-4)
- 1061 Lemaitre, B., & Hoffmann, J. (2007). The Host Defense of *Drosophila melanogaster*. *Annual Review of*
- 1062 *Immunology*, 25(1), 697–743. <https://doi.org/10.1146/annurev.immunol.25.022106.141615>
- 1063 Lesch, C., Jo, J., Wu, Y., Fish, G. S., & Galko, M. J. (2010). A Targeted *UAS-RNAi* Screen in *Drosophila*
- 1064 Larvae Identifies Wound Closure Genes Regulating Distinct Cellular Processes. *Genetics*, 186(3), 943–
- 1065 957. <https://doi.org/10.1534/genetics.110.121822>
- 1066 Lian, G., Dettenhofer, M., Lu, J., Downing, M., Chenn, A., Wong, T., & Sheen, V. (2016). Filamin A- and

Belyaeva et al

- 1067 formin 2-dependent endocytosis regulates proliferation via the canonical wnt pathway. *Development*
- 1068 (*Cambridge*), 143(23). <https://doi.org/10.1242/dev.139295>
- 1069 Linder, M., Glitzner, E., Srivatsa, S., Bakiri, L., Matsuoka, K., Shahrouzi, P., ... Sibilila, M. (2018). EGFR is
- 1070 required for FOS-dependent bone tumor development via RSK2/CREB signaling. *EMBO Molecular*
- 1071 *Medicine*, 10(11). <https://doi.org/10.15252/emmm.201809408>
- 1072 Luster, A. D., Alon, R., & von Andrian, U. H. (2005). Immune cell migration in inflammation: Present and
- 1073 future therapeutic targets. *Nature Immunology*, 6(12), 1182–1190. <https://doi.org/10.1038/ni1275>
- 1074 Makhijani, K., Alexander, B., Tanaka, T., Rulfsen, E., & Brückner, K. (2011). The peripheral nervous system
- 1075 supports blood cell homing and survival in the Drosophila larva. *Development*, 138(24), 5379-91.
- 1076 <https://doi.org/10.1242/dev.067322>
- 1077 Matsubayashi, Y., Louani, A., Dragu, A., Sánchez-Sánchez, B. J., Serna-Morales, E., Yolland, L., ... Stramer,
- 1078 B. M. (2017). A Moving Source of Matrix Components Is Essential for De Novo Basement Membrane
- 1079 Formation. *Current Biology*, 27(22), 3526-3534.e4. <https://doi.org/10.1016/j.cub.2017.10.001>
- 1080 Min, P. I., Spurney, R. F., Qisheng, T. U., Hinson, T., & Darryl Quarles, L. (2002). Calcium-sensing receptor
- 1081 activation of Rho involves filamin and rho-guanine nucleotide exchange factor. *Endocrinology*, 143(10),
- 1082 3830–3838. <https://doi.org/10.1210/en.2002-220240>
- 1083 Mitchison, T.J., and Cramer, L.P. (1996) Actin-based cell motility and cell locomotion. *Cell* 84(3)371-9).
- 1084 [https://doi.org/10.1016/s0092-8864\(00\)81281-7](https://doi.org/10.1016/s0092-8864(00)81281-7).
- 1085 Muñoz-Alarcón, A., Pavlovic, M., Wismar, J., Schmitt, B., Eriksson, M., Kylsten, P., & Dushay, M. S. (2007).
- 1086 Characterization of lamin mutation phenotypes in Drosophila and comparison to human laminopathies.
- 1087 *PloS One*, 2(6). <https://doi.org/10.1371/journal.pone.0000532>
- 1088 Ohta, Y., Suzuki, N., Nakamura, S., Hartwig, J. H., & Stossel, T. P. (1999). The small GTPase Ra1A targets
- 1089 filamin to induce filopodia. *Proceedings of the National Academy of Sciences of the United States of*
- 1090 *America*, 96(5), 2122–2128. <https://doi.org/10.1073/pnas.96.5.2122>
- 1091 Paluch, E. K., Aspalter, I. M., & Sixt, M. (2016). Focal Adhesion–Independent Cell Migration. *Annual Review*
- 1092 *of Cell and Developmental Biology*, 32(1), 469–490. [https://doi.org/10.1146/annurev-cellbio-111315-](https://doi.org/10.1146/annurev-cellbio-111315-125341)
- 1093 125341
- 1094 Perez-Hernandez, D., Gutiérrez-Vázquez, C., Jorge, I., López-Martín, S., Ursa, A., Sánchez-Madrid, F., ...
- 1095 Yañez-Mó, M. (2013). The intracellular interactome of tetraspanin-enriched microdomains reveals their
- 1096 function as sorting machineries toward exosomes. *Journal of Biological Chemistry*, 288(17), 11649–

Belyaeva et al

- 1097 11661. <https://doi.org/10.1074/jbc.M112.445304>
- 1098 Perkins, L. A., Holderbaum, L., Tao, R., Hu, Y., Sopko, R., McCall, K., ... Perrimon, N. (2015). The transgenic
- 1099 RNAi project at Harvard medical school: Resources and validation. *Genetics*, 201(3), 843–852.
- 1100 <https://doi.org/10.1534/genetics.115.180208>
- 1101 Popowicz, G. M., Schleicher, M., Noegel, A. A., & Holak, T. A. (2006). Filamins: promiscuous organizers of
- 1102 the cytoskeleton. *Trends in Biochemical Sciences*, 31(7), 411–419.
- 1103 <https://doi.org/10.1016/j.tibs.2006.05.006>
- 1104 Raab, M., Gentili, M., de Belly, H., Thiam, H.R., Vargas, P., Jimenez, A.J., Lautenschlaeger, F., Voituriez, R.,
- 1105 Lennon-Duménil, A.M., Manel, N, Piel, M. (2016). ESCRT III repairs nuclear envelope ruptures during
- 1106 cell migration to limit DNA damage and cell death. *Science*, 352(6283), 359-62.
- 1107 <https://doi.org/10.1126/science.aad7611>
- 1108 Ratheesh, A., Belyaeva, V., & Siekhaus, D. E. (2015). Drosophila immune cell migration and adhesion during
- 1109 embryonic development and larval immune responses. *Current Opinion in Cell Biology*, 36, 71–79.
- 1110 <https://doi.org/10.1016/j.ceb.2015.07.003>
- 1111 Ratheesh, A., Biebl, J., Vesela, J., Smutny, M., Papusheva, E., Krens, S. F. G., ... Siekhaus, D. E. (2018).
- 1112 Drosophila TNF Modulates Tissue Tension in the Embryo to Facilitate Macrophage Invasive Migration.
- 1113 *Developmental Cell*, 45(3), 331-346.e7. <https://doi.org/10.1016/j.devcel.2018.04.002>
- 1114 Razinia, Z., Mäkelä, T., Yläanne, J., & Calderwood, D. A. (2012). Filamins in Mechanosensing and Signaling.
- 1115 *Annual Review of Biophysics*, 41(1), 227–246. <https://doi.org/10.1146/annurev-biophys-050511-102252>
- 1116 Riesgo-Escovar, J. R., & Hafen, E. (1997). Common and distinct roles of DFos and DJun during Drosophila
- 1117 development. *Science (New York, N.Y.)*, 278(5338), 669–672.
- 1118 <https://doi.org/10.1126/science.278.5338.669>
- 1119 Riveline, D., Zamir, E., Balaban, N. Q., Schwarz, U. S., Ishizaki, T., Narumiya, S., ... Bershadsky, A. D.
- 1120 (2001). Focal contacts as mechanosensors: Externally applied local mechanical force induces growth of
- 1121 focal contacts by an mDia1-dependent and ROCK-independent mechanism. *Journal of Cell Biology*,
- 1122 153(6), 1175–1185. <https://doi.org/10.1083/jcb.153.6.1175>
- 1123 Rose, R., Weyand, M., Lammers, M., Ishizaki, T., Ahmadian, M. R., & Wittinghofer, A. (2005). Structural and
- 1124 mechanistic insights into the interaction between Rho and mammalian Dia. *Nature*, 435(7041), 513–518.
- 1125 <https://doi.org/10.1038/nature03604>
- 1126 Rouso, T., Shewan, A. M., Mostov, K. E., Schejter, E. D., & Shilo, B. Z. (2013). Apical targeting of the formin

Belyaeva et al

- 1127 diaphanous in Drosophila tubular epithelia. *ELife*, 2013(2). <https://doi.org/10.7554/eLife.00666>
- 1128 Sánchez-Sánchez, B. J., Urbano, J. M., Comber, K., Dragu, A., Wood, W., Stramer, B., & Martín-Bermudo, M.
- 1129 D. (2017). Drosophila Embryonic Hemocytes Produce Laminins to Strengthen Migratory Response. *Cell*
- 1130 *Reports*, 21(6), 1461–1470. <https://doi.org/10.1016/j.celrep.2017.10.047>
- 1131 Seth, A., Otomo, C., & Rosen, M. K. (2006). Autoinhibition regulates cellular localization and actin assembly
- 1132 activity of the diaphanous-related formins FRL α and mDia1. *Journal of Cell Biology*, 174(5), 701–713.
- 1133 <https://doi.org/10.1083/jcb.200605006>
- 1134 Sharma, P. & Allison, J.P. (2015) The future of immune checkpoint therapy. *Science* 348(6230), 56-61.
- 1135 <https://doi.org/10.1126/science.aaa8172>.
- 1136 Shigeta, M., Sanzen, N., Ozawa, M., Gu, J., Hasegawa, H., & Sekiguchi, K. (2003). CD151 regulates epithelial
- 1137 cell-cell adhesion through PKC- and Cdc42-dependent actin cytoskeletal reorganization. *Journal of Cell*
- 1138 *Biology*, 163(1), 165–176. <https://doi.org/10.1083/jcb.200301075>
- 1139 Siekhaus, D., Haesemeyer, M., Moffitt, O., & Lehmann, R. (2010). RhoL controls invasion and Rap1
- 1140 localization during immune cell transmigration in Drosophila. *Nature Cell Biology*, 12(6), 605–610.
- 1141 <https://doi.org/10.1038/ncb2063>
- 1142 Sit, S. T., & Manser, E. (2011). Rho GTPases and their role in organizing the actin cytoskeleton. *Journal of Cell*
- 1143 *Science*, 124(5), 679–683. <https://doi.org/10.1242/jcs.064964>
- 1144 Smutny, M., Ákos, Z., Grigolon, S., Shamipour, S., Ruprecht, V., Čapek, D., ... Heisenberg, C. P. (2017).
- 1145 Friction forces position the neural anlage. *Nature Cell Biology*, 19(4), 306–317.
- 1146 <https://doi.org/10.1038/ncb3492>
- 1147 Sokol, N. S., & Cooley, L. (2003). Drosophila filamin is required for follicle cell motility during oogenesis.
- 1148 *Developmental Biology*, 260(1), 260–272. [https://doi.org/10.1016/S0012-1606\(03\)00248-3](https://doi.org/10.1016/S0012-1606(03)00248-3)
- 1149 Somogyi, K., & Rørth, P. (2004). Evidence for tension-based regulation of Drosophila MAL and SRF during
- 1150 invasive cell migration. *Developmental Cell*, 7(1), 85–93. <https://doi.org/10.1016/j.devcel.2004.05.020>
- 1151 Stossel, T. P., Condeelis, J., Cooley, L., Hartwig, J. H., Noegel, A., Schleicher, M., & Shapiro, S. S. (2001).
- 1152 Filamins as integrators of cell mechanics and signalling. *Nature Reviews Molecular Cell Biology*, 2(2),
- 1153 138–145. <https://doi.org/10.1038/35052082>
- 1154 Szabo, P.A., Miron, M., & Farber, D.L. (2019). Location, location, location: Tissue residence memory T cells in
- 1155 mice and humans. *Science Immunology* 4(34), <https://doi.org/10.1126/sciimmunol.aas9673>
- 1156 Szalóki, N., Krieger, J. W., Komáromi, I., Tóth, K., & Vámosi, G. (2015). Evidence for Homodimerization of

Belyaeva et al

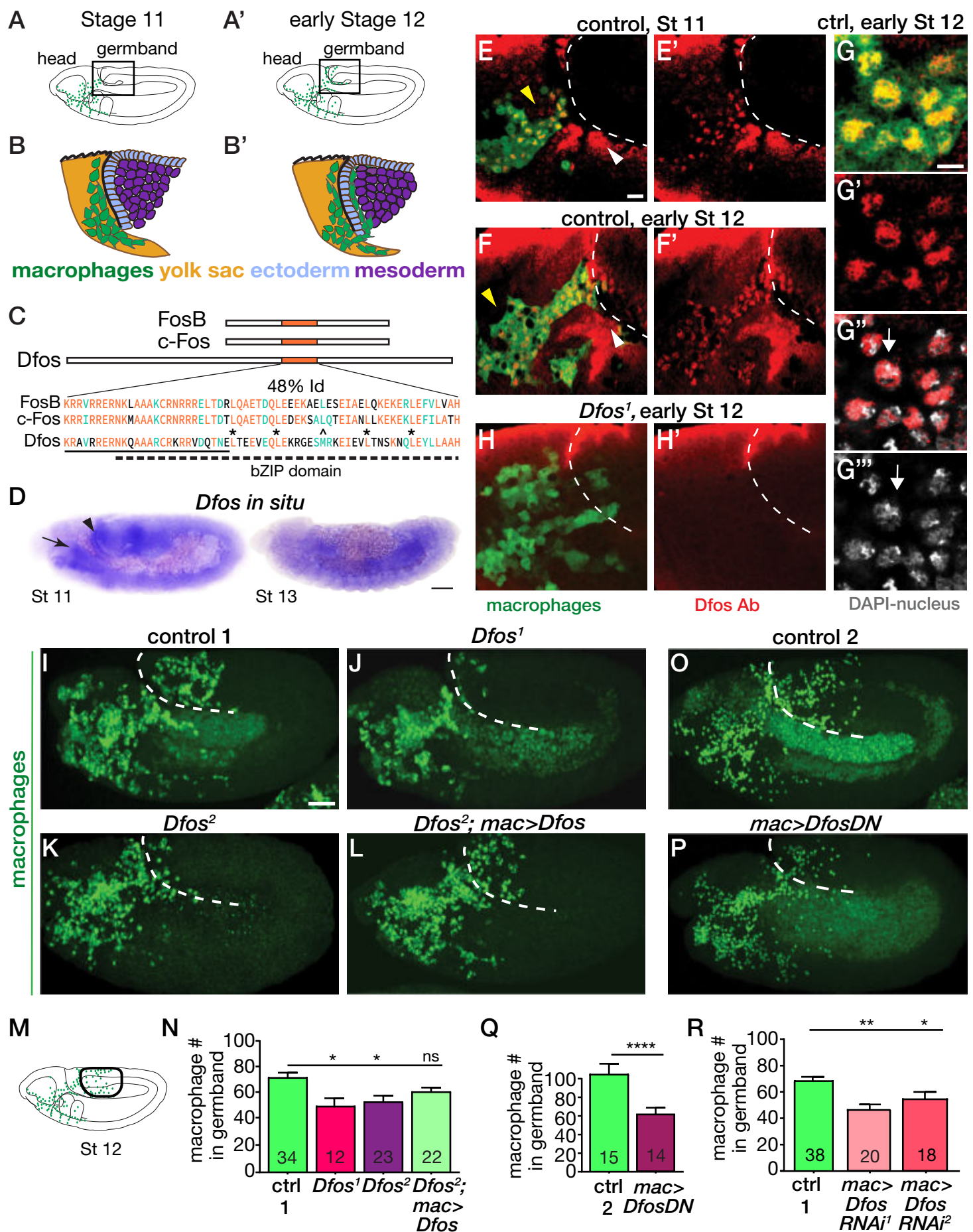
- 1157 the c-Fos Transcription Factor in Live Cells Revealed by Fluorescence Microscopy and Computer
- 1158 Modeling. *Molecular and Cellular Biology*, 35(21). <https://doi.org/10.1128/mcb.00346-15>
- 1159 Tejera, E., Rocha-Perugini, V., López-Martín, S., Pérez-Hernández, D., Bachir, A. I., Horwitz, A. R., ... Yáñez-
- 1160 Mo, M. (2013). CD81 regulates cell migration through its association with Rac GTPase. *Molecular*
- 1161 *Biology of the Cell*, 24(3), 261–273. <https://doi.org/10.1091/mbc.E12-09-0642>
- 1162 Termini, C. M., & Gillette, J. M. (2017). Tetraspanins Function as Regulators of Cellular Signaling. *Frontiers in*
- 1163 *Cell and Developmental Biology*, 5, 34. <https://doi.org/10.3389/fcell.2017.00034>
- 1164 Theret, M., Mounier, R., & Rossi, F. (2019). The origins and non-canonical functions of macrophages in
- 1165 development and regeneration. *Development*, 146(9). <https://doi.org/10.1242/dev.156000>
- 1166 Thiam, H., Vargas, P., Carpi, N., Crespo, C.L., Raab, M., Terriac, E., King, M.C., Jacobelli, J., Alberts, A.S.,
- 1167 Stradal, T., Lennon-Dumenil, A., Piel, M. (2016). Perinuclear Arp2/3-driven actin polymerization enables
- 1168 nuclear deformation to facilitate cell migration through complex environments. *Stremmel*:10997,
- 1169 <https://doi.org/10.1038/ncomms10997>
- 1170 Thurmond, J., Goodman, J. L., Strelets, V. B., Attrill, H., Gramates, L. S., Marygold, S. J., ... Baker, P. (2019).
- 1171 FlyBase 2.0: The next generation. *Nucleic Acids Research*, 47(D1). <https://doi.org/10.1093/nar/gky1003>
- 1172 Tomancak, P., Beaton, A., Weizmann, R., Kwan, E., Shu, S. Q., Lewis, S. E., ... Rubin, G. M. (2002).
- 1173 Systematic determination of patterns of gene expression during Drosophila embryogenesis. *Genome*
- 1174 *Biology*, 3(12). <https://doi.org/10.1186/gb-2002-3-12-research0088>
- 1175 Tomancak, P., Berman, B. P., Beaton, A., Weizmann, R., Kwan, E., Hartenstein, V., ... Rubin, G. M. (2007).
- 1176 Global analysis of patterns of gene expression during Drosophila embryogenesis. *Genome Biology*, 8(7).
- 1177 <https://doi.org/10.1186/gb-2007-8-7-r145>
- 1178 Tseng, Y., An, K. M., Esue, O., & Wirtz, D. (2004). The Bimodal Role of Filamin in Controlling the
- 1179 Architecture and Mechanics of F-actin Networks. *Journal of Biological Chemistry*, 279(3), 1819–1826.
- 1180 <https://doi.org/10.1074/jbc.M306090200>
- 1181 Uhlirova, M., & Bohmann, D. (2006). JNK- and Fos-regulated Mmp1 expression cooperates with Ras to induce
- 1182 invasive tumors in Drosophila. *EMBO Journal*, 25(22), 5294–5304.
- 1183 <https://doi.org/10.1038/sj.emboj.7601401>
- 1184 Vadlamudi, R. K., Li, F., Adam, L., Nguyen, D., Ohta, Y., Stossel, T. P., & Kumar, R. (2002). Filamin is
- 1185 essential in actin cytoskeletal assembly mediated by p21-activated kinase 1. *Nature Cell Biology*, 4(9),
- 1186 681–690. <https://doi.org/10.1038/ncb838>

Belyaeva et al

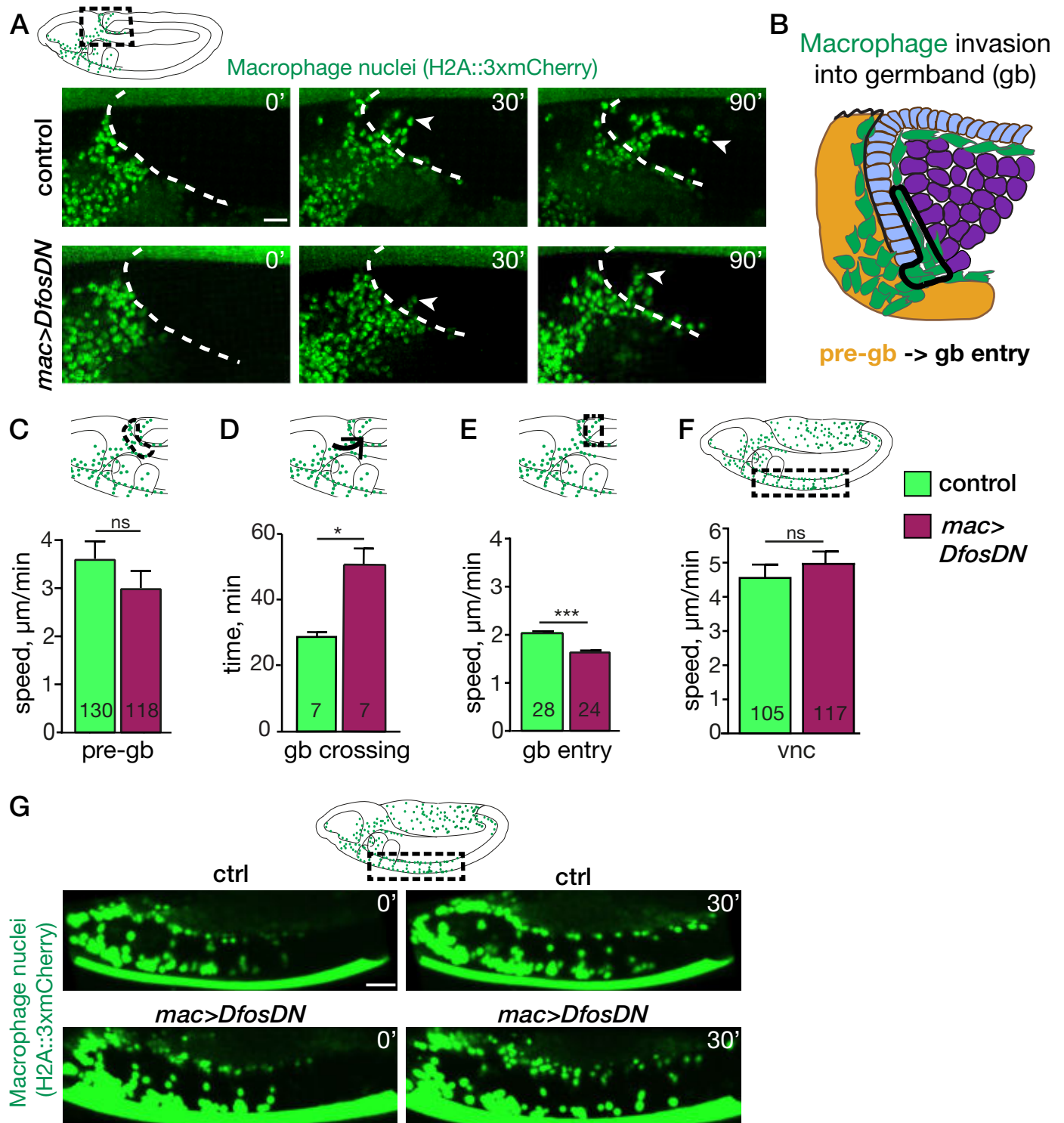
- 1187 Valoskova, K., Biebl, J., Roblek, M., Emtenani, S., Gyoergy, A., Misova, M., ... Siekhaus, D. E. (2019). A
1188 conserved major facilitator superfamily member orchestrates a subset of O-glycosylation to aid
1189 macrophage tissue invasion. *ELife*, 8. <https://doi.org/10.7554/eLife.41801>
- 1190 Vetter, I.R., & Wittinghofer, A. (2001). The guanine nucleotide-binding switch in three dimensions. *Science*
1191 294(5545), 1299-1304. <https://doi.org/10.1126/science.1062023>
- 1192 Warner, S. J., & Longmore, G. D. (2009). Cdc42 antagonizes Rho1 activity at adherens junctions to limit
1193 epithelial cell apical tension. *Journal of Cell Biology*, 187(1), 119–133.
1194 <https://doi.org/10.1083/jcb.200906047>
- 1195 Weavers, H., Evans, I. R., Martin, P., & Wood, W. (2016). Corpse Engulfment Generates a Molecular Memory
1196 that Primes the Macrophage Inflammatory Response. *Cell*. <https://doi.org/10.1016/j.cell.2016.04.049>
- 1197 Williams, M. J., Habayeb, M. S., & Hultmark, D. (2007). Reciprocal regulation of Rac1 and Rho1 in Drosophila
1198 circulating immune surveillance cells. *Journal of Cell Science*, 120(3), 502–511.
1199 <https://doi.org/10.1242/jcs.03341>
- 1200 Wintner, O., Hirsch-Attas, N., Schlossberg, M., Brofman, F., Friedman, R., Kupervaser, M., ... Buxboim, A.
1201 (2020). A Unified Linear Viscoelastic Model of the Cell Nucleus Defines the Mechanical Contributions of
1202 Lamins and Chromatin. *Advanced Science*, 7(8). <https://doi.org/10.1002/advs.201901222>
- 1203 Wood, W., Faria, C., & Jacinto, A. (2006). Distinct mechanisms regulate hemocyte chemotaxis during
1204 development and wound healing in Drosophila melanogaster. *Journal of Cell Biology*, 173(3).
1205 <https://doi.org/10.1083/jcb.200508161>
- 1206 Yáñez-Mó, M., Barreiro, O., Gordon-Alonso, M., Sala-Valdés, M., & Sánchez-Madrid, F. (2009). Tetraspanin-
1207 enriched microdomains: a functional unit in cell plasma membranes. *Trends in Cell Biology*, 19(9), 434–
1208 446. <https://doi.org/10.1016/j.tcb.2009.06.004>
- 1209 Yeung, L., Hickey, M.J., & Wright, M.D. (2018) The many and varied roles of tetraspanins in immune cell
1210 recruitment and migration. *Frontiers in Immunology*.9:1644 .[https:// doi: 10.3389/fimmu.2018.01644](https://doi.org/10.3389/fimmu.2018.01644).
- 1211 Zeitlinger, J., Kockel, L., Peverali, F. A., Jackson, D. B., Mlodzik, M., & Bohmann, D. (1997). Defective dorsal
1212 closure and loss of epidermal decapentaplegic expression in Drosophila fos mutants. *EMBO Journal*,
1213 16(24), 7393–7401. <https://doi.org/10.1093/emboj/16.24.7393>
- 1214 Zhang, X. A., Bontrager, A. L., & Hemler, M. E. (2001). Transmembrane-4 Superfamily Proteins Associate
1215 with Activated Protein Kinase C (PKC) and Link PKC to Specific β 1 Integrins. *Journal of Biological*
1216 *Chemistry*, 276(27), 25005–25013. <https://doi.org/10.1074/jbc.M102156200>

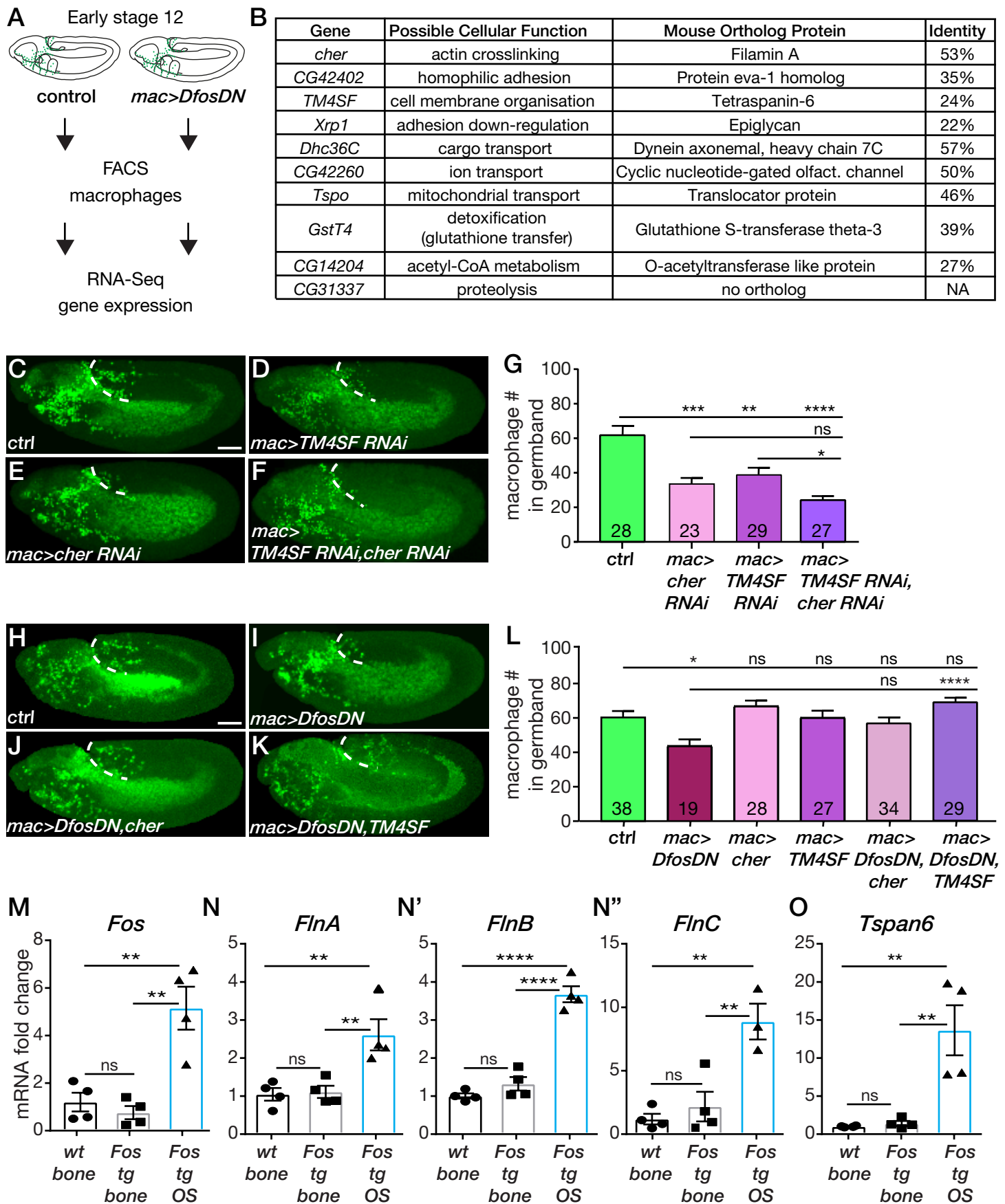
Belyaeva et al

- 1217 Zhou, J., Kim, H. Y., & Davidson, L. A. (2009). Actomyosin stiffens the vertebrate embryo during crucial
- 1218 stages of elongation and neural tube closure. *Development*, 136(4), 677–688.
- 1219 <https://doi.org/10.1242/dev.026211>
- 1220 Zimmerman, B., Kelly, B., McMillan, B. J., Seegar, T. C. M., Dror, R. O., Kruse, A. C., & Blacklow, S. C.
- 1221 (2016). Crystal Structure of a Full-Length Human Tetraspanin Reveals a Cholesterol-Binding Pocket.
- 1222 *Cell*, 167(4). <https://doi.org/10.1016/j.cell.2016.09.056>
- 1223 Zimmerman, B., Kelly, B., McMillan, B., Seegar, T., Kruse, A., & Blacklow, S. (2016). Crystal Structure of
- 1224 Human Tetraspanin CD81 Reveals a Conserved Intramembrane Binding Cavity. *Cell*, 167(4), 1041–1051.
- 1225 <https://doi.org/10.1016/j.cell.2016.09.056>
- 1226 Zwerger, M., Jaalouk, D. E., Lombardi, M. L., Isermann, P., Mauermann, M., Dialynas, G., ... Lammerding, J.
- 1227 (2013). Myopathic lamin mutations impair nuclear stability in cells and tissue and disrupt nucleo-
- 1228 cytoskeletal coupling. *Human Molecular Genetics*, 22(12), 2335–2349. <https://doi.org/10.109>
- 1229

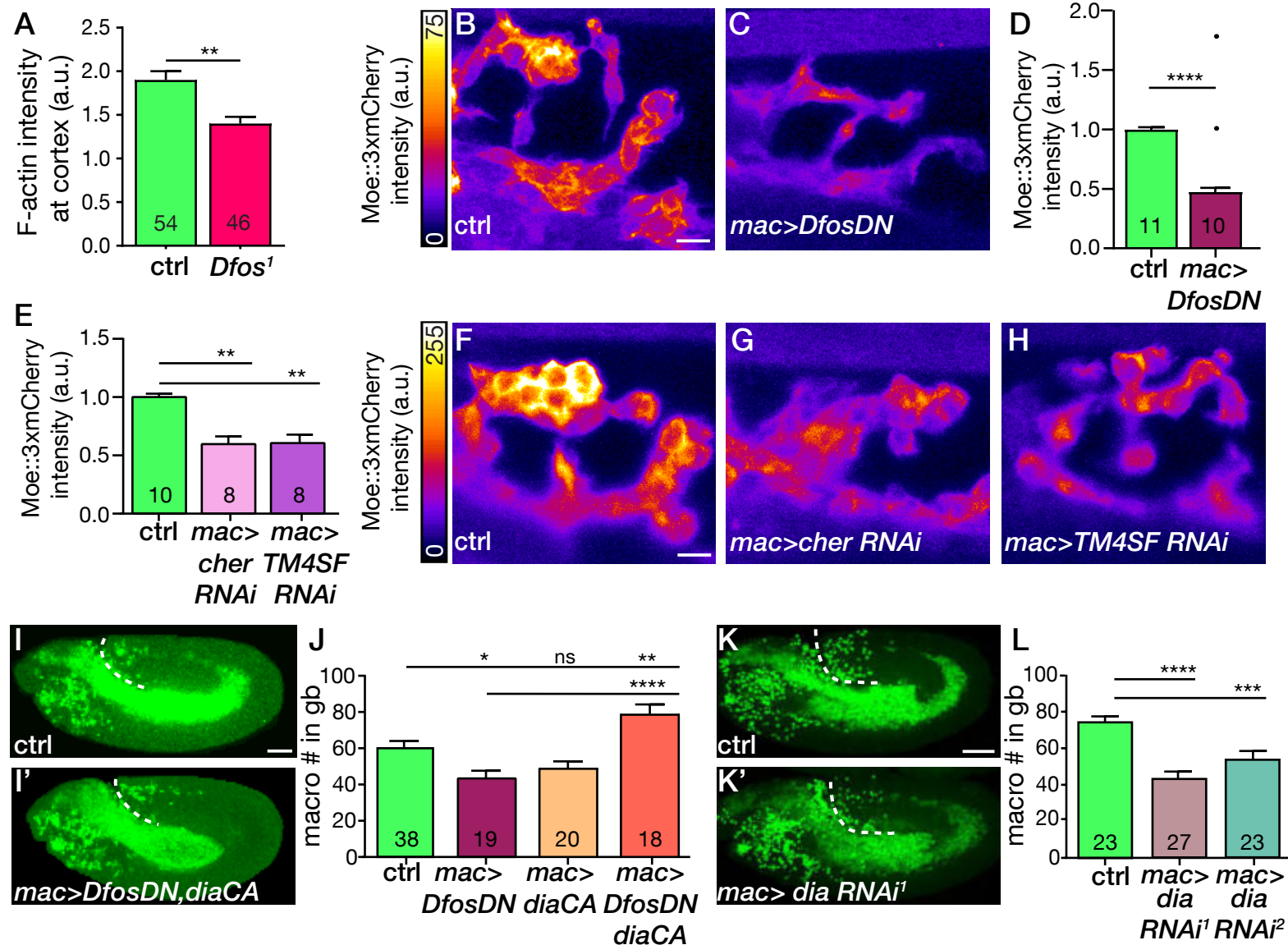


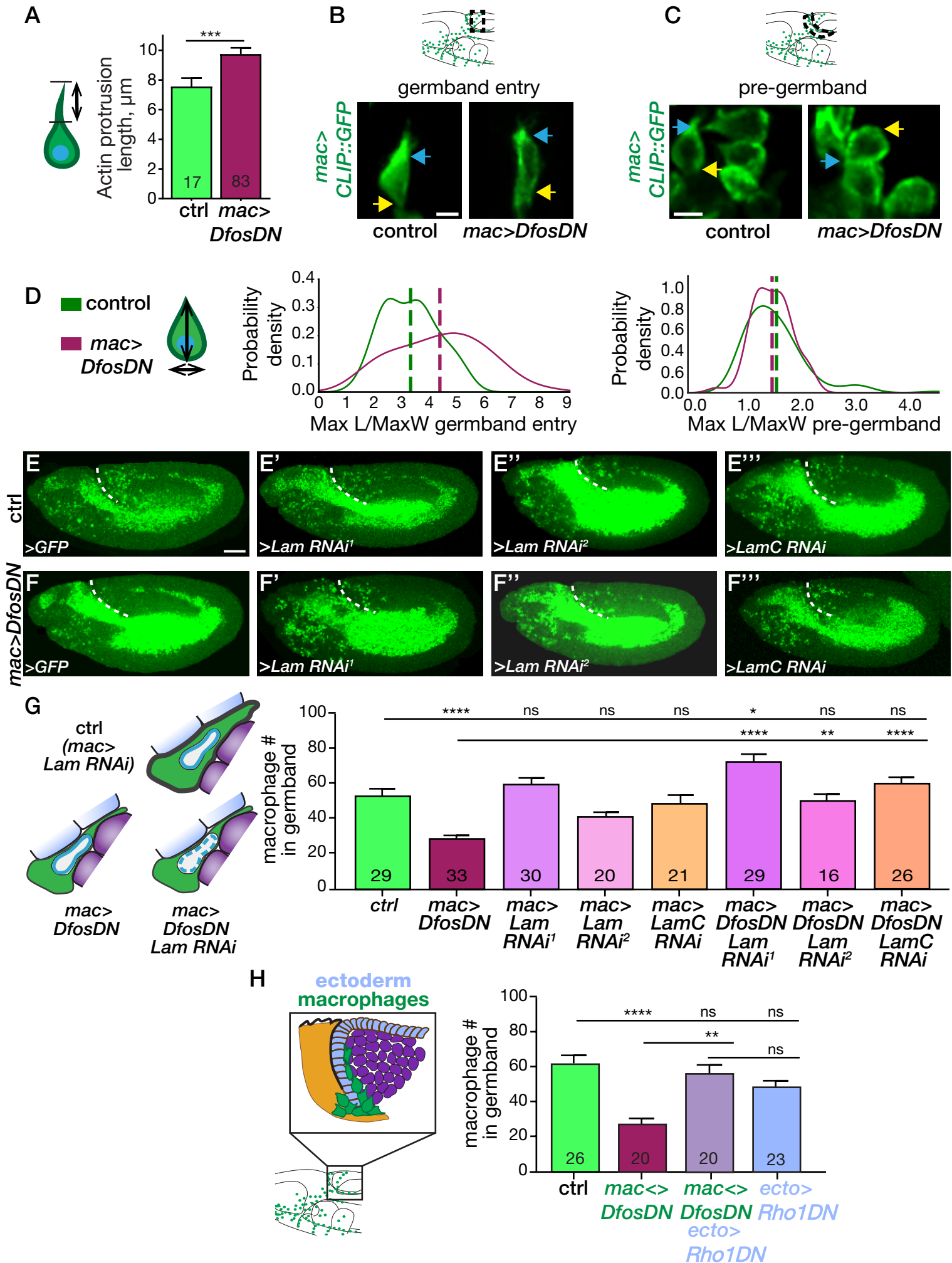
Belyaeva et al. Figure 2





Belyaeva et al, Figure 4





Belyaeva et al. Figure 6

